

Assessment and Error Analysis of Terra-MODIS and MISR Cloud-top Heights through Comparison with ISS-CATS lidar

Arka Mitra¹, Larry Di Girolamo¹, Yulan Hong¹, Yizhe Zhan¹, and Kevin J Mueller²

¹University of Illinois

²California Institute of Technology

November 23, 2022

Abstract

Cloud-top heights (CTH) from the Multiangle Imaging Spectroradiometer (MISR) and the Moderate Resolution Imaging Spectroradiometer (MODIS) on Terra constitute our longest-running single-platform CTH record from a stable orbit. Here, we provide the first evaluation of the Terra Level 2 CTH record against collocated International Space Station Cloud-Aerosol Transport System (CATS) lidar observations between 50°N - 50°S. Bias and precision of Terra CTH relative to CATS is shown to be strongly tied to cloud horizontal and vertical heterogeneity and altitude. For single-layered, unbroken, optically thick clouds observed over all altitudes, the uncertainty in MODIS and MISR CTH are -540 ± 690 m and -280 ± 370 m, respectively. The uncertainties are generally smaller for lower altitude clouds and larger for optically thinner clouds. For multi-layered clouds, errors are summarized herein using both absolute CTH and CATS-layer-altitude proximity to Terra CTH. We show that MISR detects the lower cloud in a two-layered system, provided top-layer optical depth $< \sim 0.3$, but MISR low-cloud CTH errors are unaltered by the presence of thin cirrus. Systematic and random errors are propagated to explain inter-sensor disagreements, as well as to provide the first estimate of the MISR stereo-opacity bias. For MISR, altitude-dependent wind-retrieval bias (-90 to -110 m) and stereo-opacity bias (-110 to -150 m) and for MODIS, CO₂-slicing bias due to geometrically thick cirrus leads to overall negative CTH bias. MISR's precision is largely driven by precision in retrieved wind-speed (3.7 m s⁻¹), whereas MODIS precision is driven by forward-modeling uncertainty.

1 **Assessment and Error Analysis of Terra-MODIS and MISR Cloud-**
2 **top Heights through Comparison with ISS-CATS lidar**

3 **Arka Mitra¹, Larry Di Girolamo¹, Yulan Hong¹, Yizhe Zhan^{1,2} and Kevin J. Mueller³**

4 ¹.University of Illinois, Urbana-Champaign, USA

5 ².Metservice Ltd., Wellington, New Zealand

6 ³Jet Propulsion Laboratory, California Institute of Technology, Pasadena, California, USA

7 Corresponding author: Arka Mitra (mitraarka27@gmail.com)

8 **Key Points:**

- 9 • We present the first quasi-global (50°N to 50°S) comparison of Terra cloud-top heights
10 with coincident samples from a space-based lidar.
- 11 • Using lidar as truth, Terra cloud-top height bias and precision are summarized as a function
12 of cloud geometrical and optical properties.
- 13 • With the first measurement of stereo-opacity bias (-110 to -150 m, depending on cloud
14 type), MISR cloud height error-budget is closed.
15

16 **Abstract**

17 Cloud-top heights (CTH) from the Multiangle Imaging Spectroradiometer (MISR) and the
18 Moderate Resolution Imaging Spectroradiometer (MODIS) on Terra constitute our longest-
19 running single-platform CTH record from a stable orbit. Here, we provide the first evaluation of
20 the Terra Level 2 CTH record against collocated International Space Station Cloud-Aerosol
21 Transport System (CATS) lidar observations between 50°N - 50°S. Bias and precision of Terra
22 CTH relative to CATS is shown to be strongly tied to cloud horizontal and vertical heterogeneity
23 and altitude. For single-layered, unbroken, optically thick clouds observed over all altitudes, the
24 uncertainty in MODIS and MISR CTH are -540 ± 690 m and -280 ± 370 m, respectively. The
25 uncertainties are generally smaller for lower altitude clouds and larger for optically thinner clouds.
26 For multi-layered clouds, errors are summarized herein using both absolute CTH and CATS-layer-
27 altitude proximity to Terra CTH. We show that MISR detects the lower cloud in a two-layered
28 system, provided top-layer optical depth $< \sim 0.3$, but MISR low-cloud CTH errors are unaltered by
29 the presence of thin cirrus. Systematic and random errors are propagated to explain inter-sensor
30 disagreements, as well as to provide the first estimate of the MISR stereo-opacity bias. For MISR,
31 altitude-dependent wind-retrieval bias (-90 to -110 m) and stereo-opacity bias (-110 to -150 m)
32 and for MODIS, CO₂-slicing bias due to geometrically thick cirrus leads to overall negative CTH
33 bias. MISR's precision is largely driven by precision in retrieved wind-speed (3.7 m s^{-1}), whereas
34 MODIS precision is driven by forward-modeling uncertainty.

35 **Plain Language Summary**

36 Cloud-top height (CTH) is an essential climate variable that impacts the Earth's energy
37 budget and hydrological cycle. We are greatly interested in CTHs for their possible application in
38 detecting signatures of forced climate change in the nearly two-decade long CTH record from
39 NASA's enduring mission, Terra. Since Terra has offered longevity and orbital stability, the
40 remaining criterion for a successful climate dataset is an in-depth understanding and quantification
41 of uncertainty in the data. To ascertain the accuracy of Terra sensors (a multi-view instrument,
42 MISR & a multi-wavelength instrument, MODIS), we compare a subset of their observations
43 against a lidar called CATS that operated from the International Space Station from 2015 to 2017.
44 Through involved statistical analysis, we determined that both MISR and MODIS have provided
45 us with robust CTHs, with MISR being about twice as accurate and precise as MODIS. We note
46 that the MISR error budget is self-contained and that we were able to close the error budget. Each

47 instrument demonstrates strengths and weaknesses depending on the types of clouds being
48 observed. This study has provided needed CTH error characteristics that can help inform future
49 satellite architecture for observing CTH.

50 **1 Introduction**

51 Cloud altitude feedback is an important component of cloud feedbacks (Zelinka et al.,
52 2017), with inter-model differences in cloud feedbacks being the largest source of uncertainty in
53 climate predictions (Boucher, et al., 2013; Dufresne & Bony, 2008). One of the suggested
54 techniques to lower these inter-model differences is to compare short-term model predictions with
55 accurate global trends in cloud vertical distribution from stable satellite-based sensors. However,
56 short-term trends in cloud-top height (CTH) are often quite small in magnitude and dominated by
57 natural variability in the ocean-atmosphere system (Davies et al., 2017; Geiss & Marchand, 2019).
58 Ohring et al., (2005) recommended a CTH accuracy of 150 m and a stability of 30 m/decade from
59 a satellite sensor for monitoring decadal changes in CTH. Accurate CTH is also necessary in other
60 meteorological research, such as in predicting vertical variations of freezing layers (Van
61 Dienenhoven et al., 2016). As a result, it is imperative that the error characteristics of public
62 standard CTH products be fully established and understood.

63 CTH retrievals are broadly classified as active or passive. Popular passive CTH retrieval
64 techniques include CO₂-slicing (Menzel et al., 1983), 11- μ m brightness temperature (Menzel et
65 al., 2008) and simultaneous retrieval of CTH and winds through stereo photogrammetry (Muller
66 et al., 2002). These passive techniques rely on a single-layered cloud assumption for a given field-
67 of-view – an assumption that is valid only ~75-80% of the time over the globe (Stubenrauch et al.,
68 2013). Active sensors (radars and lidars) can provide detailed hydrometeor vertical distributions,
69 unlike passive sensors. As a result, many previous studies (Marchand et al., 2007; Naud et al.,
70 2002; 2004; 2007) have employed active sensor CTH as the truth to quantify passive sensor CTH
71 errors. Those studies arrived at the consensus that multi-layered clouds can lead to large
72 differences in retrieved CTH amongst passive sensors. In those studies, and the present one, two
73 imagers onboard the Terra satellite – the Multiangle Imaging Spectroradiometer (MISR) and the
74 Moderate Resolution Imaging Spectroradiometer (MODIS) – were analyzed. Terra has provided
75 us with a consistent equator crossing time or ECT (Stubenrauch et al., 2013; Zhao et al., 2016) for
76 nearly two decades and is our longest-running stable climate record of CTH. Hence, understanding
77 the CTH error characteristics from these two instruments is essential for interpreting CTH

78 variability within their records, to shed light on their strengths and weaknesses, to combine their
79 strengths for improved CTH characterization, and to better inform future satellite missions on
80 system design choices for reducing uncertainty in CTH retrievals.

81 Collection 5 1-km and 5-km resolution CTH from the MODIS instrument on-board Aqua
82 were compared against near-coincident CALIPSO CTH globally for two months of 2006/2007 by
83 Holz et al. (2008); made possible because both these instruments are part of NASA's A-Train
84 constellation of satellites (1:30 pm ECT). Holz et al. (2008) reported globally averaged CTH
85 differences between the 1-km MODIS and CALIPSO CTH to be -1.4 ± 2.9 km (the 5-km product
86 exhibited worse accuracy and precision due to poorer resolution). Through a detailed analysis, the
87 high negative bias of CTH was found to be largely due to the presence of optically thin high clouds
88 (often, in multi-layered situations), and a failure of the-then CO₂-slicing algorithm to converge to
89 a solution in many high cloud scenes. Random errors, meanwhile, were attributed to incorrect
90 lapse-rates for marine low-level clouds and application of the brightness temperature technique for
91 high clouds (Section 4.5.2 provides an in-depth discussion of these errors). The last two issues
92 were specifically addressed in a series of improvements (Baum et al., 2012) that resulted in the
93 latest Collection 6 MODIS 1-km CTH product. Comparisons of non-polar Aqua MODIS
94 Collection 6 CTH against CALIPSO CTH showed higher deployment of CO₂-slicing than in
95 Collection 5 for single-layered cirrus (less miscasting of high clouds as low clouds) and a reduction
96 of the low-cloud positive bias from 424 m in Collection 5 to 197 m in Collection 6 (Baum et al.,
97 2012). While ostensibly the same, Terra MODIS and Aqua MODIS are subject to key differences
98 for CTH determination that stem from diurnal variability of lapse rates and cloud characteristics
99 between morning and afternoon (Eastman & Warren, 2014), as well as the absence of Band 34
100 (13.6 μ m) on Terra due to high noise. As such an independent study of Terra MODIS is also
101 necessary, as well as for validating the Collection 6 CTH product.

102 MISR employs a stereoscopic technique for determining CTH and cloud-top advection or
103 "winds", simultaneously (Mueller et al., 2013; Muller et al., 2002). The original CTH product,
104 referenced to as TC_STEREO, often reported an uncertainty of 562 m, but this was specific to the
105 error made if stereo correspondence was off by a single pixel (Moroney et al. 2002). Validation
106 against ground-based radars and lidars showed that CTH uncertainties tended to be less than 1 km,
107 irrespective of cloud height (Marchand et al., 2007; Naud et al., 2004). These studies showed that,
108 when an optically thin upper cloud overlies an optically thick lower cloud (which is often the case

109 in multi-layered situations), MISR returns the CTH of the lower cloud, provided the upper cloud
110 optical depth is less than 0.3-0.5, depending on surface type (Marchand et al., 2007). This is
111 because lower cloud layers often provide the greatest observed spatial contrast in MISR's visible
112 to near-IR images, even in the presence of thin upper clouds. TC_STEREO also produced many
113 no-retrievals, in part due to overly strict quality control. More recently, the MISR algorithm
114 underwent a series of improvements (Horváth, 2013) to generate the latest stereo product, called
115 TC_CLOUD (Mueller et al., 2013). Although direct validation of TC_CLOUD CTH against active
116 sensors has not yet been done, Horváth (2013) and Mueller et al. (2017) compared MISR winds
117 with geostationary IR atmospheric motion-vectors (AMVs) from Meteosat-9 and GOES,
118 respectively, revealing a pattern of mean and root mean-squared (RMS) differences between MISR
119 and geostationary wind heights that vary with altitude and location. (Section 4.5.1 provides an in-
120 depth discussion of these errors). Averaged globally, wind-related CTH bias relative to IR AMV
121 heights were found to be ~ -200 m, with associated precision ranging from 0.5-1 km, depending
122 on the dataset. The large deviation in the random error estimates can be attributed to the inherent
123 uncertainties of the IR AMV retrievals; however, a better estimation require precise cloud height
124 measurements, such as from a lidar.

125 The lack of a space-based active sensor with sufficient orbital overlap with Terra has so far
126 impeded a global validation of MISR and Terra-MODIS CTH. To realize our goal of validating
127 Level 2 Terra CTH, the database of 'true' active-sensor CTH came from the ISS-CATS (Yorks et
128 al., 2016). ISS-CATS or simply, CATS (Cloud- Aerosol Transport System) was a space-based
129 lidar that operated from the Japanese Experiment Module-Exposed Facility of the International
130 Space Station (ISS) between 2015-2017. Although too short-lived to be a climate record, CATS
131 was uniquely suited for a quasi-global validation of CTH from Terra-based sensors. Here we use
132 the CATS dataset to examine the error characteristics of MISR and MODIS-Terra CTHs.

133 Section 2 briefly describes the instruments, their orbits, and the data sources. Section 3
134 elucidates the collocation among CATS, MISR and MODIS pixels and quantifies the random
135 errors within our methods. Section 4 delves into CTH differences from the inter-comparison of the
136 three instruments, the global distribution of these differences, and the chief reasons behind the
137 disagreements. Concluding remarks follow in Section 5.

138 **2 Data and Instruments**

139 The flagship of NASA’s Earth Observing System (EOS), Terra, is a near-polar, sun-
140 synchronous satellite orbiting the Earth at a nominal altitude of 705 km above the surface, making
141 its equator overpasses at 10:30 am local time. MISR and MODIS are two instruments on Terra
142 that use two completely independent techniques for retrieving CTH. MISR employs a stereoscopic
143 technique using 0.67 μm (“Red” channel), 275 m resolution radiance from the three least oblique
144 angles (nadir and $\pm 26.1^\circ$) to estimate CTH (Muller et al., 2002). One advantage of a stereoscopic
145 technique over other passive CTH retrievals is that a stereo CTH is not sensitive to radiometric
146 calibration (Naud et al., 2002). The operational MISR algorithm first estimates cloud-top winds,
147 and then stereo heights for each 1.1 km pixel in a scene. The MISR data used here is the Level 2
148 TC_CLOUD Version F01_0001 orbit-level product, which provides a 1.1 km “wind-corrected”
149 CTH over a swath of width 380 km.

150 MODIS is a broad-swath (swath width ~ 2330 km) imager with 36 spectral channels that
151 has a nadir spatial resolution ranging from 250 to 1000 m, depending on the spectral channel. The
152 MISR swath lies completely within the MODIS swath. MODIS employs a CO_2 -slicing technique
153 (Menzel et al., 2008) for CTH estimation, designed to calculate the cloud top pressure (CTP) and
154 effective cloud amount for geometrically thin, single-layered mid-level and high clouds. These
155 quantities are derived from ratios of differences between cloudy and clear-sky radiances from any
156 of the following pairs: 14.2 μm /13.9 μm , 13.9 μm /13.6 μm , 13.9 μm /13.3 μm or 13.6 μm /13.3 μm ,
157 with MODIS CTP reporting the solution of the highest wavelength band-pair whose radiance
158 difference exceeds instrument noise in the individual bands. It is assumed that cloud emissivity is
159 equal for both wavelengths in the pair, an assumption better suited for ice clouds than water clouds.
160 CTP retrieval occurs at 1-km resolution, provided that at least 4 out of the 25 pixels in a 5x5 pixel
161 window surrounding it were flagged as either cloudy or probably cloudy by the MODIS cloud
162 mask and an independent pixel-level phase detection flagged ice. CTP is converted to CTH using
163 Global Data Assimilation System (GDAS) model output. For low-level (CTP > 650 hPa) or liquid-
164 phase clouds or when none of the band pairs converge to a solution, the 11- μm brightness
165 temperature (IR BT) technique estimates a cloud-top temperature (CTT) and from that, a
166 CTP/CTH is calculated from gridded model output, with provisions to adjust lapse rate for marine

167 stratus (Baum et al., 2012). The Terra MODIS CTH product used here is the Collection 6.1 Level
168 2 MOD06, which is provided in granule form at a 5-minute temporal resolution.

169 The ISS is at a mean altitude of 409 km above the Earth, revolving in a nearly circular low-
170 earth orbit with an inclination of 51.64° and completing about 16 revolutions/day. The Cloud-
171 Aerosol Transport System (CATS) (McGill et al., 2015; Yorks et al., 2016) instrument onboard
172 the ISS operated from 10 February 2015 to 30 October 2017 and consisted of two elastic
173 backscatter lasers that used a combination of low energy, high repetition rate 532 nm and 1064 nm
174 pulses to achieve greater output power than any previous space lidar (Pauly et al., 2019). Although
175 instrument failure prevented its multiple intended operating modes, nadir-only information was
176 retained. During its run, CATS data was continuously downlinked at 60 m vertical and 350 m
177 horizontal resolution (except for loss-of-signal periods), and then pre-processed, geo-located and
178 calibrated to produce CATS Level 1 attenuated total backscatter and depolarization ratio profiles
179 (Yorks et al., 2016). Geophysical parameters derived from Level 1 information is compiled into
180 5-km resolution Level 2 data, including depolarization ratio and attenuated backscatter, along with
181 their layer-integrated values. The CATS layer-detection algorithm follows the Cloud-Aerosol
182 Lidar with Orthogonal Polarization (CALIOP) (Vaughan et al., 2005; Yorks et al., 2015), with the
183 main difference being that CATS applied threshold-based feature-detection on 5-km backscatter
184 profiles at 1064 nm, as opposed to 532 nm for CALIOP. CATS layer-detection operated only at a
185 single 5 km horizontal resolution (60 m vertical), whereas the CALIOP algorithm successively
186 runs at fine to coarse horizontal resolutions ranging from 5 to 80 km in order to detect progressively
187 tenuous layers (Vaughan et al., 2009). Cloud-aerosol feature-mask discrimination and cloud phase
188 detection are identical to CALIOP. Details of these techniques can be found in the CATS
189 Algorithm Theoretical Basis Document (Yorks et al., 2015). CATS Version 2.01 Level 2 Product
190 used in this study provided values at every lidar range-gate associated with successful layer-
191 discrimination. For this study, only range-gates with cloudy feature-masks were considered.

192 **3 Collocation Methodology**

193 For an accurate inter-comparison between instruments, one needs to be able to compare
194 spatially and temporally concurrent observations, due to the transient nature of atmospheric
195 conditions. In our case, MODIS has the widest swath and CTH is stored in 5-minute granules at 1
196 km resolution; whereas, MISR, with a much narrower swath nestled within the MODIS swath,

197 provides CTH at 1.1 km resolution that are stored per orbit. This enables a one-to-one collocation
198 between MODIS and MISR pixels. However, CATS has a narrow Ground Instantaneous Field-of-
199 View (GIFOV) of 14.38 m diameter, which is equivalent to its swath-width since it does not scan
200 cross-track. Each CATS Level 2 datum has an along-track resolution of 5 km. Thus, when overlap
201 of the Terra and ISS orbits did happen, it was possible to have multiple MODIS and MISR pixels
202 neighboring a single CATS Level 2 point. Here, we choose a one-to-one collocation between each
203 CATS point and the nearest-neighbor MISR and MODIS points, since the spatial correlation length
204 for cloud properties can be of the order of tens or even a few hundreds of kilometers (Marchand,
205 2012). This choice is further justified later in this section. The mean geolocation difference for
206 collocated pixels was found to be ~ 0.4 km for both CATS-MISR and CATS-MODIS collocation.
207 To find the collocated set of data, the following choices were made:

- 208 1) Only those MISR data points are selected that lie within a distance of 380 km (MISR swath
209 width) and whose observation time is within 5 minutes (to later accommodate MODIS
210 granule time) from a given CATS point. From within this chosen subset of MISR data, a
211 nearest-neighbor search finds the nearest point lying within a 1 km distance from the CATS
212 data point, if any. If collocated points are found, only then is a MODIS search conducted.
- 213 2) MODIS granules that lie within a 5-minute window of a given CATS-MISR datum are
214 selected for a nearest-neighbor search. When the point is found, MISR and MODIS CTH,
215 MODIS CTH detection technique, and CATS cloud layer-heights, associated 1064 nm
216 backscatter, surface elevation, and geolocation are extracted and stored. The altitude of the
217 center of the highest lidar range-gate having cloudy feature mask in a column is taken as
218 the cloud-layer height, whereas the base of the cloud-layer is taken to be the height of the
219 range-gate, which is followed by at least 5 successive clear-featured gates.

220
221 Figure 1 shows an example of successful collocation among all three instruments from 14th
222 March 2016, over southeast Asia. Figure 1a shows the three different swaths along with CTH from
223 MISR and MODIS, with the collocated points marked in black. Figure 1b-1d shows the same scene
224 in MODIS RGB, 1.38 μ m reflectance and 11 μ m brightness temperature, respectively, whereas
225 Figure 1e depicts the CATS-retrieved vertical profile of cloud-masked attenuated backscatter,
226 along with collocated MISR and MODIS CTH. This particular scene was chosen as it has low-
227 lying cumuli, both with and without cirrus cover. For single-layered clouds, as between 21°N-

228 22°N, there is greater agreement between MISR and MODIS CTH. However, the presence of
229 cirrus between 22°N-24°N (see lidar in 1b, cooler cloud tops in 1c and 1.38 μm imagery in 1d)
230 leads to severe disagreements between MISR and MODIS, with MISR CTH consistently picking
231 up the lower cumuli and MODIS retrievals being highly variable. The range wherein collocations
232 are feasibly within the MISR swath extends from 21°N and 24°N so MISR CTH are only shown
233 therein. All heights are with respect to the World Geodetic System 1984 (WGS84) ellipsoid.

234 An intuitive sense for the collocation process can be formed from Figure 2. Figure 2a shows
235 a highly zoomed-in view of a patch of MISR and MODIS geolocations from the same scene as in
236 Figure 1, with a set of CATS pixels cutting through. The search for collocated data is conducted
237 within the 1-km radii circular windows that are marked around each CATS geolocation in Figure
238 2a (the circles are merely representative and not to scale). With navigation errors (~ 100 m),
239 collocation differences (~ 400 m), and mismatches in pixel-size amongst instruments (~ 1 km \times 1
240 km vs ~ 14 m \times 5 km, it is the local CTH variations below these scales that introduce uncertainty
241 in comparing MISR or MODIS CTH with CATS. To quantify this random error, we found all the
242 MISR and MODIS data that lay within circular regions for each of the 9538 CATS points that
243 satisfied the co-location conditions for the year 2016 and examine CTH variations as a function of
244 radius of the circular region. For example, the histograms of the standard deviations in CTH within
245 each region of 1-km radius (number of neighbors at least 2), denoted as σ_{MISR} for MISR and σ_{MODIS}
246 for MODIS, is shown in Figure 2b. Both σ_{MISR} and σ_{MODIS} peak at 0.1 km, with their mean values
247 being 0.2 and 0.5 km, respectively. Thus, the CTH of each collocated point from MISR and
248 MODIS can be taken to be generally representative of CTH of all other observations within a 1
249 km circle centered around the CATS data point, with an uncertainty of about 200 m for MISR and
250 500 m for MODIS. There is also a mismatch in resolution between MISR/MODIS (~ 1 km) and
251 CATS (5 km), as well as wind displacement of clouds during the maximum allowed time-interval
252 between observations of 5 minutes in our coincidence criteria (e.g., a high wind speed of ~ 30 m/s
253 can displace clouds close to 10 km in five minutes). Thus, local CTH variations over scales up to
254 ~ 10 km also introduce uncertainty in comparing the CTH between MISR or MODIS with CATS.
255 Thus, σ_{MISR} and σ_{MODIS} are calculated for progressively increasing search radii up to 10 km and
256 plotted in Figure 2c. It is observed that both σ_{MISR} and σ_{MODIS} exhibit asymptotic behavior with
257 increasing distances, reaching 0.3 km and 0.8 km, respectively. These values can be interpreted as
258 an upper limit of CTH error owing to our method of collocation. The error is larger for MODIS

259 because MISR is generally more sensitive to lower clouds (owing to the higher spatial contrast
260 they offer relative to thin cirrus) than MODIS, where variability in CTH and emissivity are smaller
261 compared to high and midlevel clouds – evident, for example, in Figure 1 (e).

262 In most of this study going forward, the topmost CATS cloud layer height is compared
263 against MODIS and MISR CTH, since satellite derived CTH is often associated with the height of
264 the topmost cloud layer. However, to investigate the sensitivity of sensors to individual layers, the
265 closest CATS layer to MISR/MODIS CTH is studied in Section 4.4.

266 **4 Results and Causes of CTH Differences**

267 By applying the collocation method mentioned above, 36 months (February 2015-October
268 2017) of collocated MISR, MODIS and CATS CTH have been compared spanning a quasi-global
269 domain. In total, 51622 collocated (clear + cloudy) points were collected, among which, 27% were
270 rejected as flagged clear by MODIS; 12% are outside the region of MISR swath with valid
271 retrievals; 22% reported MISR CTH “no-retrievals” – that is MISR stereo failed owing to a lack
272 of contrast (e.g., over clear sky ocean); and 2% did not have valid CATS cloud-layer retrieval
273 where MODIS and MISR retrieved a CTH. Over land, (provided enough surface texture), MISR
274 stereo can retrieve surface elevation as stereo height. Such features have been dealt with in our
275 study by subtracting surface elevation from MISR stereo heights for every collocated point and
276 further, only retaining such points in our analysis whose surface-elevation-corrected stereo heights
277 were at least greater than 562 m – the value used by MISR for cloud designation (Mueller et al.
278 2013). The CATS pixel-level surface elevation from the 1x1 km USGS GMTED2010 digital
279 elevation map (DEM) is used for this purpose. Finally, our analysis on valid CTH retrievals was
280 conducted on a dataset of 18986 cloudy points.

281 **4.1 Global and Regional Biases from MISR, MODIS and CATS Inter-comparison**

282 Figure 3 shows the global distribution of all 18986 collocated CATS, MISR and MODIS
283 data. Unless otherwise noted, CATS CTH will refer to the topmost CATS cloud-layer altitude.
284 Figure 3 shows that there is a much higher frequency of collocation near the 50° latitudes in both
285 hemispheres, due to greater swath overlap of Terra with ISS. This study is restricted to an inter-
286 comparison over the tropics and midlatitudes since the ISS orbit does not venture further poleward.
287 Also, Figure 3 shows that CATS detects the presence of a lot more very high CTH (e.g., West

288 Pacific warm pool region) than MODIS or MISR, owing to the lidar's ability to detect optically
289 thinner clouds. MISR detects a lower mean CTH than CATS or MODIS, because MISR stereo is
290 sensitive to spatial texture in multi-angular views, which is greater for lower, textured clouds, even
291 under cirrus. The textured nature of the radiance field in the Western Pacific warm pool was
292 recently examined by Hong & Di Girolamo (2020), demonstrating that the texture of ice-above-
293 liquid clouds was only slightly smoother than liquid-only clouds owing to the fact that cirrus in
294 the region are generally optically thin. Hence, the spatial contrast observed by MISR has the largest
295 contribution from liquid clouds under conditions of ice-over-liquid clouds in the region.

296 Figure 4 shows the latitudinal dependence of CTH differences between the three
297 instruments, expressed as (a) CATS-MODIS, (b) CATS-MISR and (c) MODIS-MISR. In each
298 individual panel, the median CTH differences for every 5 degrees latitude interval from 60°N –
299 60°S were plotted at the mid-point of each corresponding interval. Each figure shows the median
300 CTH difference for the bin for all clouds in black, CATS single-layered clouds in red and multi-
301 layered clouds in blue. The error bars for each point signify the median absolute deviation, a robust
302 statistic that is directly proportional to statistical dispersion but is resilient to the presence of
303 outliers in a non-normal distribution. For CATS-detected multi-layered clouds, there are at least 2
304 cloud layers present, with the layers being separated by a vertical distance of at least 600 m (10
305 range-gates). The last panel (d) depicts the latitudinal distribution of number of samples. As can
306 be seen from Figure 4a-4c, the largest differences in median CTH for all clouds (in black) are
307 observed about the equator in the tropical regions (between 20°N – 20°S), owing to the
308 contribution from multi-layered clouds. Large differences near the tropics were also noticed in the
309 CALIOP and Aqua MODIS CTH difference record by Holz et al. (2008) and is due to the frequent
310 presence of high and optically thin cirrus, often overhanging low and optically thick cumuli (e.g.,
311 Li et al., 2015; Stubenrauch et al., 2013). Moreover, from Figure 4, the median deviations for both
312 CATS-MODIS and CATS-MISR CTH for multi-layered scenes is much greater than single-
313 layered clouds. This increase for multi-layered scenes is more pronounced for CATS-MISR than
314 for CATS-MODIS, because MODIS and CATS are theoretically more sensitive to higher clouds
315 under cloud overlap, whereas, MISR is more sensitive to textured low clouds, even in the presence
316 of overlying optically thin cirrus (e.g., Naud et al., 2007). The comparatively modest increase in
317 MODIS for multi-layered clouds can be attributed to MODIS underestimating the semi-transparent
318 top layer height, when the lower layer is optically thick (Menzel et al., 2015). The jump for multi-

319 layered clouds for MODIS-MISR is striking in its absence, suggesting median MODIS and MISR
320 CTH are closely similar; this will be explored in upcoming sections.

321 **4.2 Height of the Top Cloud Layer**

322 To further investigate CTH differences, histograms for the three instrument pairs have been
323 plotted in Figure 5. The CTH differences here are (a and d) MODIS-CATS, (b and e) MISR-CATS
324 and (c and f) MISR-MODIS, respectively. 100 equal-sized bins between -20 km and 20 km, and
325 between -5 km and 5 km, have been used for the top- and bottom-panel, respectively, with all
326 histograms centered at zero. CATS CTH is the topmost CATS layer height. While analyzing these
327 results, one must be mindful that different instruments' CTH might be due to cloud occurrence at
328 different altitudes; this issue of cloud overlap in the interpretation of CTH differences is examined
329 in Section 4.4. In Figure 5 and in figures to follow, an inverted system of axes in red has been
330 added showing mean CATS top-layer height in each histogram bin, each point further color-coded
331 by mean CATS top-layer layer-integrated backscatter (γ), for all scenes in that bin. A lower γ
332 denotes an optically thinner cloud. A CATS $\gamma = 0.02 \text{ sr}^{-1}$ approximately corresponds to mean layer-
333 integrated optical depth (OD) of 0.8 (linear regression between CATS Level 2 OD with integrated
334 backscatter). In each Figure 5 subplot, the purple line signifies CATS high clouds (CTH > 5 km),
335 the blue line signifies CATS low clouds (CTH < 5 km), while the dashed black line signifies all
336 collocated points. Of these 18986 points, 10315 were high clouds and the rest low clouds.

337 Figure 5 shows that high absolute CTH differences in all cases arise from the presence of
338 optically thin, high cloud layers. The peaks of the distributions for all clouds (dashed black) in the
339 top panel are at (a) -800 m for MODIS-CATS, (b) -420 m for MISR-CATS and (c) -80 m for
340 MISR-MODIS. These peaks exist where γ is largest. There exist prominent tails in all, extending
341 up to about -15 km for MODIS-CATS and MISR-CATS and up to -12 km for MISR-MODIS.
342 These long tails are due to optically thin, high clouds, with $\gamma < 0.02 \text{ sr}^{-1}$ and with mean CATS top-
343 layer height > 10 km. Most cases in the MODIS-CATS (76%) and the MISR-CATS (89%)
344 distributions involve negative CTH differences (i.e., MODIS and MISR CTH below CATS top-
345 layer height). Most positive MODIS-CATS differences are for scenes with CATS top-layer height

346 below 7 km and $\gamma > 0.03 \text{ sr}^{-1}$ (OD ~ 1.2). Most positive MISR-CATS differences, however, arise
347 from high clouds (CTH ~ 10 km), and moderate optical thickness ($\gamma \sim 0.02 \text{ sr}^{-1}$, OD ~ 0.8).

348 As evident in Figure 5 and in other figures to follow, CTH differences follow
349 approximately Gaussian distributions, exhibiting well-defined modes, with variable offsets from
350 zero. So for a consistent inter-comparison between these datasets, we shall denote the distributions
351 (restricted to absolute differences < 5 km) by their Mode and Mode standard deviation (σ), where
352 $\sigma = \frac{FWHM}{2\sqrt{2\ln 2}}$ (assuming normality), and FWHM is the Full Width at Half-Maximum for our
353 distribution. These statistics are chosen over a simple mean or variance of the data, because they
354 are not skewed by outliers, that arise due to differing sensitivities of CATS, MISR and MODIS to
355 different clouds in a scene. We note that such a mode and σ for the MODIS-CATS and MISR-
356 CATS CTH difference distributions represent the bias and precision of MODIS and MISR CTH,
357 assuming CATS CTH as the truth and the errors to be normally distributed about the mode. As we
358 analyze the many parameters on which these sensitivities depend (e.g., top-layer properties and
359 multi-layering), we shall gain more insight into these primary modes and outliers.

360 For high cloud scenes (purple lines, Figure 5), there is much disagreement between the
361 three instruments. From Figures 5a and 5d, MODIS high-cloud CTH bias = -1200 m and precision
362 = 1080 m, while from Figures 5b and 5e, MISR high cloud bias = -540 m and precision = 590 m.
363 This difference in the MODIS and MISR distribution arises primarily from scenes where multiple
364 cloud layers are present and the instruments are identifying different layers to report height, with
365 MISR being more sensitive to lower clouds, while MODIS CTH is dependent on optical and
366 geometrical properties of the multiple cloud layers in the scene (Holz et al., 2008; Naud et al.,
367 2002; Naud et al., 2007; Stubenrauch et al., 2013). Further MODIS errors arise due to optically
368 thin, geometrically thick cirrus, as the assumption of an infinitesimally thin cloud layer is central
369 to the effectiveness of CO₂-slicing. The probabilities of MISR and MODIS detecting the true
370 height of a CATS high cloud to within ± 1 km is nearly equal at about 15%, in spite of MISR not
371 being as sensitive as MODIS to optically thin cirrus. MODIS underestimation of high CTH for
372 multi-layered scenes seems to be the primary reason behind this phenomenon.

373 There is much agreement between the instruments for low clouds (blue line, Figure 5).
374 From Figures 5b and 5e, MISR-CATS CTH difference exhibits a sharp distribution, with MISR

375 low-cloud bias = -320 m and precision = 250 m. MISR-CATS low cloud CTH differences fall
376 within 0 and -600 m 74% of the time. In comparison, MODIS low cloud CTH (Figure 5a and 5d)
377 exhibits a bias = 40 m and precision = 730 m, with 14% of MODIS-CATS differences below -2
378 km and 29% of differences above 0. For low clouds, MODIS uses the IR BT technique with
379 latitudinally varying climatological lapse rates (Baum et al., 2012). Significant deviations from
380 these lapse rates is a source of uncertainty. Holz et al. (2008) and Harshvardhan et al. (2009)
381 demonstrated that the Collection 5 MOD06 product was overestimating CTH by over 2 km in
382 cases where a low-lying liquid phase cloud was present over the ocean, particularly in the presence
383 of strong temperature inversions, due to poor representation in ancillary data. As rectification, the
384 Collection 6 MOD06 started using zonally-averaged “apparent 11- μm brightness temperature (BT)
385 lapse rates” from a combination of CALIOP CTH and modeled sea-surface temperatures to better
386 capture boundary-layer lapse rates (Baum et al., 2012). This improvement manifests itself in the
387 absence of the hump in positive MODIS-CATS differences that was observed in MODIS-
388 CALIPSO differences reported in Figure 8 of Holz et al. (2008).

389 Despite MISR applying stereoscopy and MODIS a radiometric technique, the two passive
390 sensors do produce reasonable agreement in CTH. The MISR-MODIS CTH difference distribution
391 (Figure 5c and 5f) has Mode = -400 m and $\sigma = 680$ m. 62% of all MISR-MODIS CTH differences
392 lie between ± 2 km, with an optically thick top-layer at a mean altitude of about 5 km, and the
393 spread of the distribution is attributable to the natural variability of clouds in a scene and the
394 different sensitivities of MISR and MODIS to this variability (Section 3). About 36% of CTH
395 differences is constituted by differences between 0 and -2 km, mostly for top layers of cloud with
396 integrated backscatter larger than 0.02 sr^{-1} and with heights < 10 km, and is associated with MODIS
397 IR BT CTH overestimation for stronger temperature inversions (note, IR BT technique is applied
398 for all but high and mid-level ice clouds). A sizeable portion of MISR-MODIS differences in both
399 high and low cloud scenes (25% and 36%, respectively) have positive values up to +2 km. Positive
400 MISR-MODIS bias (mean difference = 0.6 km) for optically thin clouds is primarily due to

401 optically thin and geometrically thick cirrus (mean geometric depth of top layer in the 0 to +2 km
402 interval from CATS ~ 1.2 km) and this role of OD on bias will be explored in the next section.

403 **4.3 Optical Depth of the Top Cloud Layer**

404 Figure 5 suggests that as one moves from large negative top-layer CTH differences to zero,
405 there is a general tendency of the top-cloud layer to be lower and optically thicker for MISR and
406 MODIS. As one moves from zero to positive CTH differences, the top layer starts to be slightly
407 higher, with only a modest reduction in the mean backscatter. These tendencies are consistent with
408 our knowledge of the three CTH retrieval techniques. This is especially true for CATS and
409 MODIS, because their retrievals are highly dependent on cloud optical properties. An optically
410 thicker top layer of cloud represents an opaque or a nearly opaque atmospheric column to the lidar,
411 which leads to rapid attenuation of the lidar signal near the cloud top. This represents a strongly
412 emissive cloud-top layer, hence the retrieved CTP (in case of the CO₂-slicing technique) or the
413 CTT (in case of the 11 μ m-BT technique) is very close to actual values. However, for more
414 transmissive cases, CTT and BT can diverge substantially, resulting in lower CTH under typical
415 conditions; higher under atypical conditions (i.e., surface, or lower cloud layer being cooler than
416 the cloud-top layer). The CO₂-slicing approach hinges on an assumption of a thin cloud layer, and
417 any geometrical depth (especially accompanied by low optical depth) can lead to underestimation
418 of CTH, through an overestimation of CTP. Smith & Platt (1978) estimated errors ~50 hPa in CTP
419 for a cloud of ~100 hPa depth and CO₂-slicing is generally likened to a centre of mass problem
420 (Menzel et al., 2008), with CTP errors co-varying with optical depth into the cloud (i.e., CTP close
421 to true cloud-top for optically thick, and closer to the geometric centre for optically thin cases). As
422 a result, the CTH difference in these cases, is a function of the vertical distribution of extinction in
423 the cloud layer, as well as temperature throughout the column. On the other hand, although MISR
424 makes use of a stereoscopy, MISR-CATS differences are also expected to depend on the vertical
425 distribution of single scattering properties of the top cloud layer, as well as its horizontal
426 distribution that gives rise to the spatial contrast for stereoscopy to work. For a single layer cloud,
427 the contrast is expected to emerge over some depth of the cloud layer that is likely deeper than a
428 lidar-derived height. For an optically thin upper cloud overlapping an optically thick lower cloud,
429 the largest spatial contrast may well emerge from the lower cloud layer, allowing stereo to retrieve

430 the CTH of the lower cloud layer. The exact relationship of this ‘*stereo-opacity bias*’ with the 3D
431 distribution of cloud optical properties has yet to be quantified from theory or experiments.

432 To gauge the impact of the top-layer cloud optical properties on the retrieval of CTH for
433 low and high clouds from MODIS and MISR, Figure 6 shows histograms of CTH differences for
434 the three instrument pairs with 100 equal-width bins between -5 km and +5 km, for optically thick
435 top cloud layers ($\gamma > 0.02 \text{ sr}^{-1}$) in purple and optically thin top cloud layers ($\gamma < 0.02 \text{ sr}^{-1}$) in blue.
436 The top panel (Figure 6a-6c) is for CATS high clouds (CATS CTH > 5 km), while the lower panel
437 (Figure 6d-6f) is for CATS low clouds (CATS CTH < 5 km). Based on the observed relationships
438 between CTH differences and backscatter in the previous figures, $\gamma = 0.02 \text{ sr}^{-1}$ (OD~0.8) is simply
439 chosen as a distinction between optically thick and optically thin cloud.

440 From Figure 6a, the MODIS-CATS CTH difference for optically thin, high topmost cloud
441 layer shows much variation, especially for negative differences. The issues faced by the CO₂-
442 slicing technique for semi-transparent clouds are many-fold, including errors due to cloud
443 geometrical depth and the presence of lower cloud layers (Smith & Platt, 1978; Wielicki &
444 Coakley, 1981; Wylie & Menzel, 1989), leading to MODIS optically thin high clouds bias = -1160
445 m and precision = 1020 m, with 84% of MODIS-CATS CTH differences being negative. MODIS
446 optically thick high cloud CTH has bias = -280 m and precision = 730 m, and the MODIS-CATS
447 distribution has a sharper peak. From Figure 6b, MISR optically thick high cloud bias = -440 m
448 and precision = 470 m, with the MISR-CATS distribution being less noisy than the corresponding
449 MODIS-CATS distribution, although the larger MISR bias suggests that MODIS heights are closer
450 to the lidar cloud top than MISR for these clouds. The distributions for optically thick (mode = -
451 20 m, $\sigma = 610 \text{ m}$) and thin high clouds (mode = -320 m, $\sigma = 640 \text{ m}$) for the MISR-MODIS
452 difference (Figure 6c) are both symmetrical about their modes.

453 For CATS low clouds, from Figure 6d, the MODIS-CATS distribution shows two distinct
454 peaks – the optically thin cloud distribution (bias = -440 m, precision = 600 m) and the optically
455 thick cloud distribution (bias = 500 m, precision = 430 m) are both consistent with the limitations
456 of the IR BT technique and with the Collection 6 improvements. Optically thin clouds being more
457 transmissive, allow more IR radiation from closer to the warm surface to reach the satellite, leading
458 to negative CTH bias, whereas the positive bias for optically thicker or more emissive clouds

459 presumably owes its origin to a larger deviation of true boundary-layer lapse rates from the
460 Collection 6 climatological lapse rates. However, it needs to be noted that the bias for both
461 optically thin and thick low clouds show a marked improvement from Collection 5 (Figure 11b of
462 Baum et al. 2012). The MISR-CATS distributions (Figure 6e) for optically thick low clouds (bias
463 = -280 m, σ = 260 m) and optically thin low clouds (bias = -320 m, precision = 310 m) exhibit a
464 slight dependence of MISR low cloud retrieval on the optical depth (see discussion above). This
465 will be explored in the next section after we have quantified the relationship of CTH differences
466 with multi-layering. The distributions for optically thick and thin low clouds for the MISR-MODIS
467 difference (Figure 6f) closely resemble that of the MODIS-CATS CTH distributions as the
468 dependence of MISR CTH on OD is considerably lesser than that of MODIS CTH.

469 To recap, the previous two sections have quantified CTH differences between sensors,
470 examined how these differences depend on the top layer properties, and provided evidence of
471 significant contribution from cloud overlap in explaining these differences. The next section
472 isolates those contributions and, in their absence, examines the depth within the cloud that these
473 instruments are most sensitive to.

474 **4.4 Multi-layered Clouds**

475 Past research (Marchand et al., 2007; Naud et al., 2007; Naud et al., 2004; Holz et al., 2008)
476 and the previous sections have flagged multi-layered clouds as leading to passive sensor CTH
477 errors. To quantify this, histograms of CTH differences is shown in Figure 7, based on multi-
478 layering for CATS high cloud (CTH > 5 km), with 100 equal-sized bins between -20 km and 20
479 km. The purple line indicates single-layered high cloud, and the blue line indicates at least more
480 than one layer (with minimum vertical separation of 600 m) and the black line is a histogram for
481 all high clouds. Moreover, since an optically thick high cloud can completely attenuate the lidar
482 signal (preventing low-cloud detection), we further restrict single-layered clouds to those scenes
483 with CATS Percentage Opacity lesser than or equal to 0.5. CATS reports a Percentage Opacity,
484 defined as the fraction of “opaque” (no surface detection) 350 m-resolution Level 1 samples that
485 constitute a Level 2 5-km datum. A value of 0 signifies ‘all profiles transparent’, while 1 signifies
486 ‘all profiles opaque’. Note, the term ‘Percentage Opacity’ should not to be confused with a measure
487 of cloud optical depth; rather it should be thought of as a measure of the sub-pixel transmittance

488 homogeneity of a CATS datum. This threshold is applied to reduce the occurrence of multi-layered
489 broken clouds, which can make comparisons between the different product resolutions tenuous.

490 From Figure 7, the greatest occurrence of negative MODIS-CATS (Figure 7a) and MISR-
491 CATS CTH differences (Figure 7b) are found in multi-layered cases where the top-layer has $\gamma <$
492 0.02 sr^{-1} and a mean CTH of more than 10 km. In multi-layered cases, CATS top-layer CTH and
493 MODIS CTH are within 1 km of each other for only about 10% of the time, while it is only 4%
494 for CATS top-layer CTH and MISR CTH. Compared to that, negative differences less than -2 km
495 are observed in 7% of all single-layered cases in the MODIS-CATS distribution (bias = -1160 m,
496 precision = 510 m) and a total of 5% in the MISR-CATS distribution (bias = -720 m, precision =
497 460 m), with these high negative values also due to semi-transparent high clouds (same as multi-
498 layered scenes). It is worth noting that even in single-layered cases, we cannot rule out the
499 presence of an optically thick lower layer below (Percentage Opacity = 0.5 can mean a maximum
500 of 7 out of the 14 350-m Level 1 profiles in the CATS datum were transparent).

501 For MODIS-CATS and MISR-CATS differences, positive values are found as well,
502 primarily for CATS single-layered clouds. While these positive values comprise 11% of the
503 MODIS-CATS and 9% of the MISR-CATS distribution, it is worth noting that these values extend
504 up to +5 km for MODIS-CATS, and are due to optically thick top-layers with mean CTH of 7.8
505 km; while for MISR-CATS, these positive differences extend up to about +2.5 km, but are due to
506 optically thick top-layers with mean CTH of 11.6 km. Positive MISR height bias for high clouds
507 is due to wind-retrieval bias at those heights (Horváth, 2013); positive MODIS bias for high clouds
508 requires an independent discussion provided in Section 4.6.

509 MISR-MODIS CTH differences (Figure 7c) does not show striking differences between
510 single-layered (Mode = -80 m, $\sigma = 670 \text{ m}$) and multi-layered scenes (Mode = -80 m, $\sigma = 710 \text{ m}$),
511 except in the tail. Overall, MISR and MODIS sense the same cloud to within 1 km of each other
512 nearly 30% of the times – 25% for multi-layered and 32% of all single-layered scenes. These
513 scenes constitute the primary peak of the distributions and have a top-layer mean backscatter of
514 0.012 (OD~0.5) and mean altitude of 11.8 km.

515 For multi-layered cases, it is also necessary to quantify which cloud layer the passive sensor
516 is sensitive to; hence, separate histograms of differences between MODIS and MISR CTH and

517 CATS Layer 1 (top layer) and Layer 2 (bottom layer) heights are plotted in Figure 8, for scenes
518 where CATS detected just two distinct layers of clouds at least 600 m apart. The difference
519 between MISR or MODIS CTH and the closest CATS layer height is plotted in black. Figure 8
520 shows that MISR is highly sensitive to CATS Layer 2 (with bias = -400 m and precision = 350 m),
521 seen in the tight overlap of the ‘MISR - CATS Layer 2’ and ‘MISR - Closest CATS Layer’ curves.
522 For scenes where MISR detected CATS Layer 2, the mean and SD of the top-layer γ (OD) were
523 0.002 (~0.08) and 0.0052 (~0.18), respectively. MISR detection of CATS Layer 1 has bias = -820
524 m and precision = 850 m), with a mean and SD top-layer γ (OD) of 0.01 (~0.4) and 0.009 (~0.3),
525 respectively. This suggests the possibility of a threshold OD necessary for MISR stereo to detect
526 thin cirrus overhanging a textured low cloud, as was suggested in Marchand et al. (2007). One
527 might expect this threshold to be a function of sun-satellite geometry, texture, and resolution,
528 requiring future investigations using observations and radiative transfer modeling.

529 Figure 8b shows that MODIS CTH tends to lie between the two layers as indicated by large
530 negative and positive tails for Layer 1 and Layer 2, respectively, and being strongly aligned with
531 neither. For small negative MODIS-CATS differences, CATS Layer 1 is preferred (bias = -1200
532 m, precision = 1190 m) as the closest CATS layer (CO₂-slicing – negative bias); while for small
533 positive MODIS-CATS CTH differences, CATS layer 2 (bias = 20 m, precision = 850 m) is
534 preferred (BT technique – positive bias). This is consistent with Sections 4.2 and 4.3.

535 **4.5 CTH Bias and Precision by Instrument**

536 Sections 4.2-4.4 investigated the effects of cloud parameters (top-layer height and optical
537 depth, and multi-layering) on the error characteristics of MISR and MODIS CTH retrievals, by
538 assuming CATS CTH to be the truth; these results are summarized in Table 1. However, to
539 constrain our error estimates further, we seek to remove the inherent uncertainty in the collocation
540 process, as well as eliminate the possibility of having multiple layers in a scene. To this end, for
541 the determination of instrument bias and precision, we now restrict ourselves to only single-layered
542 CATS Level 2 profiles with Percentage Opacity = 1 (i.e., all constituent Level 1 profiles that went
543 into the 5-km product being opaque); suggesting an absence of broken, multi-layered clouds and
544 with minimum layer-integrated OD ~ 3 (the OD at which a CATS signal is completely attenuated)
545 and where the absolute values of MISR-CATS and MODIS-CATS differences are less than 2.5

546 km (approximately, the largest FWHM from results above). This leaves us with ~6000 data points,
547 each for both MISR and MODIS investigation.

548 MISR and MODIS bias (offset of the distribution mode from 0) and precision (σ from the
549 FWHM approach) are calculated and summarized in Table 2 for all, high (CATS CTH > 5 km),
550 mid-level (10 km > CTH > 5 km) and low-level (CTH < 5 km) clouds. Moreover, as summarized
551 in Table 1, MISR and MODIS bias and precision exhibits variable dependence on the height and
552 OD of the cloud layer, and to investigate further, Figure 9 shows the distribution of MISR (Figure
553 9a) and MODIS (Figure 9b) bias and precision (1σ errors-bars) with altitude (for every 2 km
554 interval) for the same scenes. Each such interval contains a minimum of 150 collocated pixels (~7-
555 10 independent scenes). The mean CATS integrated backscatter from cloud top to 300 m below
556 cloud top, γ_{300} , is also shown for each bin. It is readily apparent from both Table 2 and Figure 9
557 that MISR exhibits lower bias and greater precision than MODIS CTH, and that both MISR and
558 MODIS precision deteriorates with increasing altitude of the cloud. A detailed discussion of the
559 error budget for MISR and MODIS CTH are discussed in the next two sub-sections.

560 **4.5.1 MISR CTH Errors**

561 The MISR bias reported in Table 2 arises from three principal sources – bias in co-
562 registration of oblique radiances with nadir, wind-retrieval bias, and a stereo-opacity bias (retrieval
563 of stereo height at a depth into the cloud due to low extinction near the top). We assume CATS
564 CTH to be unbiased. Sources of random error that determine the overall MISR CTH precision
565 include geo-registration errors of MISR imagery, correspondence errors of conjugate cloud
566 features in MISR imagery, random wind-retrieval errors, and random sub-pixel CTH variability
567 due to geo-collocations (~300 m from Section 3). We assume the random error in CATS CTH to
568 be the result of equal probability of successful and failed detection over the depth of one range-
569 gate: thus, contributing a random error of 30 m. Globally, MISR image geo-registration error is
570 estimated to be 0.05 ± 0.25 pixels, which translates to height errors of about 30 ± 140 m (Davies
571 et al., 2007; Jovanovic et al., 2007).

572 Wind-retrieval errors also propagate to height errors, although these contributions have
573 been reduced from the TC_STEREO to TC_CLOUD product (Horváth, 2013; Lonitz & Horváth,
574 2011; Mueller et al., 2017). Comparison of MISR near-surface heights to ground targets allows

575 for the evaluation of CTH errors due to the combined effects of registration, correspondence, and
576 DEM errors, as done in Horváth (2013). We repeated their analysis using MISR data between
577 50°N and 50°S, finding the mode in height to be = -40 m and $\sigma = 170$ m, using the FWHM
578 approach. These values are similar to the values (mean height error = -31 m, RMS error = 171 m)
579 reported in Horváth (2013).

580 If the bias was not a function of wind speed, then we would conclude for the overall cloud
581 samples used in Table 2 that the stereo-opacity bias is $-280 \text{ m} + 40 \text{ m} = -240 \text{ m}$ (-260 for high
582 clouds; -200 m for low clouds). However, based on the analysis of Horváth (2013), wind errors do
583 vary with altitude based on comparisons with geostationary wind data, with an along-track wind
584 bias of $\sim 1 \text{ m s}^{-1}$ for low clouds and $\sim 1.2 \text{ m s}^{-1}$ for high clouds, respectively (cross-track winds are
585 essentially unbiased). Using $\sim 90 \text{ m}$ height error for each 1 m s^{-1} error in along-track wind-speed
586 (Mueller et al., 2017; Table 1), these wind-errors translate to CTH errors of $\sim 90 \text{ m}$ for low clouds
587 and $\sim 110 \text{ m}$ for high clouds. Thus, we deduce that the stereo-opacity bias is $\sim -110 \text{ m}$ ($= -200 \text{ m} +$
588 90 m) and $\sim -150 \text{ m}$ ($= -260 + 110 \text{ m}$) for low and high clouds, respectively. The difference in
589 stereo-opacity bias between high and low clouds is likely due to lower clouds having larger γ_{300}
590 (i.e., greater extinction coefficients in the upper parts of the cloud; Figure 9a).

591 For the MISR CTH precision budget, we noted earlier that the MISR CTH co-
592 registration/correspondence/DEM precision = 170 m and that the maximum CTH geolocation
593 precision of our method = 300 m. But, since we are dealing with Percentage Opacity = 1 in this
594 section, we expect the geolocation-related variations in heights to be much smaller here, and our
595 overall observed precision of 370 m may be almost entirely dictated by the precision of MISR
596 stereo. Here, it should be noted that our observed precision is about twice as good as was reported
597 in both Horváth (2013) and Mueller et al. (2017), and is most likely due to the highly precise CTH
598 that a lidar is able to offer (taken here as 30 m) compared to the IR AMV heights used in those
599 studies. Assuming geolocation-related height error = 0 m, and the overall MISR precision from
600 Table 2 to be 373 m, the MISR wind-height precision = $\sqrt{370^2 - 170^2 - 30^2} = 330 \text{ m}$ (360 m
601 and 250 m for high and low clouds, respectively). Using the 90 m (m s)^{-1} wind-height error
602 proportionality again, we get an overall MISR wind speed precision of 3.7 m s^{-1} (4.0 m s^{-1} and 2.8
603 m s^{-1} for high and low clouds, respectively). Our MISR wind speed precision estimates backed out
604 through MISR-CATS comparison are remarkably close to those determined by both Horváth

605 (2013) and Mueller et al. (2017), thus providing closure. This result also implies that the MISR
606 operational quality assurance procedures, most notably the required agreement (and subsequent
607 averaging) of forward and aft-derived height estimates, are filtering and improving the accuracy
608 of raw stereo retrievals to an extent that mitigates the difficulty of obtaining heights from highly
609 dynamic or poorly textured clouds.

610 **4.5.2 MODIS CTH Errors**

611 A similar accounting of MODIS CTH bias and precision is not strictly possible as MODIS
612 uses *a priori* assumptions and ancillary data to determine CTH. Its errors covary with the
613 departures from these assumptions and deviations from reality in the ancillary data. The errors in
614 IR sensors have been historically quantified as CTP errors (Menzel et al., 2015; Wielicki &
615 Coakley, 1981), although in recent literature (Baum et al., 2012; Holz et al., 2008), CTH errors
616 have been quantified by comparing low-level and single-layered clouds against lidar. For example,
617 from Figure 12 of Baum et al. (2012), we can estimate the bias and precision (FWHM method as
618 above) to be -1100 m and 930 m, respectively, for single-layered cirrus, and a bias and precision
619 of 200 m and 550 m for low clouds. The corresponding values of bias and precision for high and
620 low clouds in Table 2 are quite similar, even though we define high and low clouds differently
621 than that study. The MODIS bias (Table 2) seems to be largely due to high clouds, which goes
622 back to systematic bias in the CO₂-slicing technique, which employs an infinitesimally thin cloud
623 assumption. In these high cloud samples (optically thick cirrus), the negative bias presumably
624 arises because optically thick cirrus also tends to be geometrically thick, leading to CO₂-slicing
625 underestimating CTH. Again, owing to the choice of Percentage Opacity = 1, MODIS precision is
626 assumed to be mostly unaffected by collocation errors, and originates from the forward modelling.

627 Systematic CTH overestimation by MODIS for low clouds and underestimation for semi-
628 transparent high clouds is due to the retrieval techniques it employs and cannot be explained by
629 just top-layer height, OD and overlap. For MODIS, the low and high cloud distinction used here
630 nearly coincides with the 75th percentile heights (green-dashed lines in Fig. 9b) where IR BT and
631 CO₂-slicing techniques are applied, whereas mid-level clouds employ both. As a result, the bias

632 and precision of the two techniques can be roughly estimated by MODIS bias and precision for
633 high and low clouds (Table 2).

634 To investigate the MODIS CTH bias and precision for the two CTH techniques, Figure 10
635 presents histograms for MODIS-CATS (10a and 10c) and MISR-MODIS (10b and 10d) CTH
636 differences for all CATS high (CTH > 5 km) clouds (top panel) and single-layered high clouds
637 (bottom panel). Only high cloud retrievals are chosen to focus on scenes where CO₂-slicing is
638 preferred, but IR BT is still possible. A simple pressure-based distinction is not applicable as CO₂-
639 slicing is only reserved for ice clouds. Aqua-MODIS phase flag is understood to accurately
640 determine ice phase 65-80% of the time globally, through inter-comparisons with
641 CLOUDSAT/CALIPSO data, with >90% agreement for multiple surface types for single-phase
642 clouds (Marchant et al., 2016; Platnick et al., 2017). From Figure 10, we see that 57% of all
643 collocated high clouds and 70% of single-layered high clouds were retrieved using CO₂-slicing, in
644 keeping with the improvements of Collection 6 MOD06 updates aimed at increasing frequency of
645 CO₂-slicing retrievals (Baum et al., 2012). In both high and single-layered high clouds, the smallest
646 differences are associated with CO₂-slicing for MODIS-CATS and with IR BT technique for the
647 MISR-MODIS. This discrepancy is because CO₂-slicing is more sensitive to optically thin high
648 clouds than MISR and has a mean CTH closer to mean CATS CTH in most cases (especially,
649 single-layered high clouds), as shown in Figure 5. However, due to reasons explained earlier,
650 MODIS often detects mid-tropospheric CTH about 3-5 km above MISR CTH. Large MODIS-lidar
651 differences occur for IR BT technique, as noted in previous studies (Holz et al., 2008; Naud et al.,
652 2004), for semi-transparent high clouds (OD < 1), where MODIS opts for the IR BT technique
653 over the more precise CO₂-slicing. The mean MODIS CTH error associated with the application
654 of the IR BT technique is found to be -5.8 km overall for scenes with CATS CTH > 5 km, with
655 CATS mean top-layer backscatter less than 0.02 sr⁻¹ and mean top-layer height greater than 10 km.
656 For CATS single-layered high clouds, mean CTH error from the application of IR BT is -2.3 km.

657 For MODIS-CATS difference (Figure 9a and 9c), there exists a noticeable hump in the
658 distribution for positive values and is associated with optically thick, single-layered high clouds
659 (as in Figure 6a) with top-layer backscatter greater than 0.01 sr⁻¹ and CTH between 5-10 km. From
660 Figure 9, this hump is clearly associated with CO₂-slicing and not IR BT and is difficult to explain
661 based on the information at hand. CO₂-slicing is subject to many sources of errors – instrument

662 noise, uncertainties in calculating clear-sky radiances, assumption of constant emissivity in band-
663 pairs used to calculate CTP and deviations from constant lapse rates. Apart from these, there may
664 be two more sources of error for the present data. Firstly, CATS, unlike the CALIOP lidar used in
665 Holz et al. (2008), employs a single horizontal resolution (5 km) for layer-detection and is known
666 to miss extremely tenuous cirrus layers during daytime (Rajapakshe et al., 2017). As a result, it
667 might be possible that MODIS 1-km CTH can detect small, thin higher cirrus that CATS might
668 miss. Secondly, a problem endemic to Terra MODIS, but not with Aqua-MODIS used in Holz et
669 al. (2008), is that one of the bands used in the CO₂-slicing – Band 34 (13.6 μm) – remains unused
670 due to severe noise, effectively reducing the algorithm to just 14.2/13.9 and 13.9/13.3 μm ratios
671 (most sensitive to pressure regimes of 100-450 hPa and 550-650 hPa, respectively), instead of the
672 full suite of options (Menzel et al., 2008). Hence, in this analysis alone, 73.1% of all CO₂-slicing
673 retrievals for high clouds and 78% for single-layered high clouds were from the 14.2/13.9 μm
674 band-pair, while the remainder came from 13.9/13.3 μm band-pair. The important 35/33 (13.9/13.6
675 μm) band pair, most sensitive to mid-level clouds and cloud edges (Menzel et al., 2015), is missing
676 and is a possible reason for overestimation of mid-level CTH.

677 **5 Conclusions**

678 Terra is our longest running single-platform mission with a stable ECT for cloud top
679 heights (CTH), now spanning more than 2 decades. Its long record from a stable orbit makes it
680 valuable in climate research and in data assimilation in reanalysis products. Of course, its scientific
681 application requires well characterized errors in the public geophysical products produced by the
682 Terra mission. Here we have used the ISS CATS lidar to quantify the error characteristics of
683 MODIS and MISR CTHs from Terra, producing the first quasi-global evaluation of these errors
684 from space-based lidar. Ample collocated (< 1 km) and concurrent (< 5 minutes) MODIS, MISR
685 and CATS samples were retrieved during the CATS 2015-2017 period for robust statistics. While
686 CATS top-layer CTH is taken as truth in our analysis, the CATS-detected lower-level cloud tops
687 underlying thin upper-level clouds were also used to examine MODIS and MISR CTH error
688 characteristics – an approach that proved to be central in our understanding of MISR and MODIS
689 CTH. Generally, we find that MISR and MODIS CTH errors are larger in the tropical regions and

690 smaller in the midlatitudes, and are strong functions of cloud type, defined by cloud height, optical
691 depth and multi-layering, as summarized in Tables 1 and 2.

692 For CATS CTH < 5 km (single or multi-layered), MISR and MODIS CTH biases and
693 precisions (bias \pm precision) are -320 ± 250 m and 40 ± 720 m, respectively. MISR CTH bias
694 changes little with optical depth (Figure 6), but a reduction of MISR CTH bias to -240 m for
695 unbroken, single-layered and opaque low clouds is observed (Table 2). In contrast, MODIS CTH
696 bias for low clouds (hence, IR BT technique) is highly dependent on optical depth with average
697 bias of -440 m for thin clouds ($\gamma < 0.02$ sr⁻¹ or OD < 0.8) and of $+500$ m for thick clouds ($\gamma > 0.02$
698 sr⁻¹) (Table 1). This dichotomy occurs because for optically thinner (more transmissive) clouds,
699 the IR BT technique senses a thermal signature of the warmer surface, whereas, for high OD (more
700 emissive) clouds, there is presumably greater lapse rate deviation from the climatology used in
701 Collection 6 MOD06 product. When considering the subset of unbroken, single-layered, and
702 opaque low clouds, MODIS CTH bias is $+60$ m (Table 2), with the positive bias for more emissive
703 clouds dominating, as low clouds tend to be thicker on average in our dataset.

704 For CATS CTH > 5 km (single or multi-layered), MISR and MODIS CTH biases are -540
705 ± 590 m and -1200 ± 1080 m, respectively. For both MISR and MODIS, high cloud biases do tend
706 to vary with optical depth. MODIS CTH bias is -1160 m for thin high clouds ($\gamma < 0.02$ sr⁻¹) and $-$
707 280 m for thick clouds ($\gamma > 0.02$ sr⁻¹). Low opacity near cloud-top in geometrically thick clouds
708 leads to underestimation of MODIS CTH as CO₂-slicing technique assumes an infinitesimally thin
709 single-layered cloud solution. Similarly, the MISR CTH bias is -680 m for high clouds with $\gamma <$
710 0.02 sr⁻¹ and -440 m for those with $\gamma > 0.02$ sr⁻¹, suggesting the presence of a stereo-opacity bias –
711 the depth into the cloud in which spatial contrast is established in the emerging radiation field.
712 This study provides the first assessment of the MISR stereo-opacity bias, estimated here to range
713 between -110 and -150 m for clouds sampled in this study. It is larger for higher altitude clouds
714 owing to the optically thinner nature of cloud tops for higher altitude clouds.

715 For CATS-retrieved multi-layered clouds, which are often thin cirrus overlying thicker
716 clouds, CTH comparisons are more complicated. Both passive sensors severely underestimate top-
717 layer CTH, MISR by -820 ± 850 m and MODIS by -1200 ± 1190 m. These large biases necessitate
718 us to adopt a “closest layer” approach (i.e., comparing passive-sensor CTH to closest CATS layer

719 height). For two-layered cases, MISR is found to be sensitive to the lower cloud layer, with MISR
720 CTH errors for this lower layer being -400 ± 350 m. This is almost identical to MISR single-
721 layered low cloud bias and precision, suggesting that MISR low CTH accuracy is independent of
722 the presence of a high, thin cirrus. The mean top-layer OD when MISR detects the higher layer is
723 found to be 0.4 ± 0.3 , agreeing with the result from Marchand et al. (2007). This is indicative of
724 an opacity threshold for stereo detection, a parameter which would presumably be a function of
725 sun-satellite geometry and spatial contrast. MODIS underestimates top-layer CTH by greater than
726 1 km due to the CO₂-slicing technique converging at a higher-pressure solution, when an optically
727 thin (OD < 0.8) cloud is present. As a result, MODIS produces more midlevel CTH than MISR
728 and MISR-MODIS CTH differences have generally low absolute values.

729 Optically thick, single-layered, unbroken clouds allow us to neglect random collocation
730 errors (~ 300 m) for a complete error budget analysis for MISR stereo. Unlike MODIS, the MISR
731 CTH error budget is self-contained since it does not rely on external ancillary products. MISR
732 underestimates CTH for these clouds by -280 ± 370 m. Contributors to the bias are estimated as:
733 (a) bias in imagery co-registration and feature correspondence (~ -40 m), (b) MISR stereo-opacity
734 bias (-110 to -150 m, dependent on cloud altitude) and (c) MISR wind-correction bias (-90 to -110
735 m, also dependent on altitude). Random errors in this dataset are largely due to wind-driven errors
736 (330 m for all samples, 250 m for low and 360 m for high clouds). Based on our estimated wind-
737 height precision, we were able to provide an independent estimate of MISR wind-speed precision
738 of 3.7 m s⁻¹ (2.8 m s⁻¹ and 4.0 m s⁻¹ for low and high clouds, respectively). These values are quite
739 similar to the findings of Horváth (2013) and Mueller et al. (2017). Thus, we conclude that we
740 have essentially achieved closure on the MISR CTH error budget.

741 Similarly, MODIS underestimates CTH by -540 ± 690 m for these optically thick, single-
742 layered, and unbroken clouds in our dataset. While it is difficult to exactly quantify, the largest
743 contributor to MODIS CTH bias is the CO₂-slicing underestimation for geometrically thick cirrus.
744 MODIS CTH random errors are due to inherent uncertainties in the forward model and reliance
745 on external ancillary datasets. Since CO₂-slicing is best suited for thin cirrus, application of IR BT
746 for high clouds (when CO₂-slicing does not converge to solution), can still lead to erroneous
747 results, as discussed in Holz et al., (2008). However, compared to Collection 5, improvements of
748 Collection 6 low-cloud CTH from the marine boundary-layer correction, as well in high-cloud

749 retrievals from adopting CO₂-slicing technique more frequently (Baum et al., 2012), have indeed
750 led to a substantial reduction in errors in MODIS CTHs.

751 Based on the findings presented here, it is clear that MISR and MODIS CTHs can be
752 combined for improved interpretation of CTH variability, particularly in multi-layered conditions.
753 Our findings also point to recommendations for future satellite architecture designs that have CTH
754 as a target product, such as the Aerosol and Cloud, Convection and Precipitation (ACCP) mission
755 called out in NASEM (2018). As each of these sensors (lidar, IR, multi-view) occupies a niche
756 that cannot be replaced by the others alone, these sensors on a single-orbit taking observations of
757 the same physical reality can improve the short-comings of each by creating fused datasets that
758 complement each other and provide greater insight to CTH variability than any of these sensors
759 operating alone. Also, our analysis and closure of the MISR CTH error budget has several
760 implications for future stereo-enabled technological designs. Since the largest contributor to the
761 error budget are wind-driven errors, removing this error can be achieved by flying two (or more)
762 multi-view imaging systems in close proximity and in close formation. This would allow for the
763 same scene to be viewed at the same time; hence removing wind-driven errors. Improving
764 resolution would also improve the precision in the stereo CTH (an instrument resolution of ~100
765 m would contribute ~60 m to the precision budget, assuming MISR viewing geometry). We
766 recommend that detailed 3D radiative transfer modeling be undertaken to fully understand the
767 nature of the remaining stereo-opacity bias – how it varies with sun-satellite geometry and cloud
768 micro- and macro-physical properties.

769

770 **Acknowledgments, Samples, and Data**

771 This research was supported under MISR project contract 147871 with the Jet Propulsion
772 Laboratory, California Institute of Technology. Partial support from the NASA ACCESS program
773 under contract NNX16AMO7A is also acknowledged. The MISR data were obtained from NASA
774 Langley Research Center Atmospheric Sciences Data Center
775 (<https://l0dup05.larc.nasa.gov/opensdap/misr1213/MISR/contents.html>). The MODIS data were
776 obtained through the Level 1 and Atmosphere Archive and Distribution System of NASA Goddard
777 Space Flight Center (<https://ladsweb.modaps.eosdis.nasa.gov/archive/allData/61/>). The CATS
778 data was downloaded from the NASA Langley Research Center's ASDC DAAC
779 (<https://opensdap.larc.nasa.gov/opensdap/CATS/>). We are thankful to the NASA MODIS, MISR
780 and CATS teams for supplying the documentation and tools, especially the MISR toolkit
781 (<https://nasa.github.io/MISR-Toolkit/html/index.html>). Data was stored and computation was
782 conducted on the University of Illinois, Urbana-Champaign School of Earth, Society, and
783 Environment (SESE) computer cluster, Keeling. We are thankful to Catherine Moroney for
784 providing the data used to calculate MISR stereo errors for near-surface retrievals. We also thank
785 Puja Roy and Jesse Loveridge for the many fruitful discussions and inputs.

786 **References**

- 787 Baum, B. A., W. P. Menzel, R. A. Frey, D. C. Tobin, R. E. Holz, S. A. Ackerman, A. K. Heidinger,
788 and P. Yang (2012), MODIS Cloud-Top Property Refinements for Collection 6, *Journal of*
789 *Applied Meteorology and Climatology*, 51(6), 1145–1163, doi:10.1175/jamc-d-11-0203.1.
- 790 Boucher, O., D. Randall, P. Artaxo, C. Bretherton, G. Feingold, P. Forster, V.-M. Kerminen, Y.
791 Kondo, H. Liao, U. Lohmann, P. Rasch, S.K. Satheesh, S. Sherwood, B. Stevens, and X.Y.
792 Zhang, 2013: Clouds and aerosols. In *Climate Change 2013: The Physical Science Basis.*
793 *Contribution of Working Group I to the Fifth Assessment Report of the Intergovernmental*
794 *Panel on Climate Change.* T.F. Stocker, D. Qin, G.-K. Plattner, M. Tignor, S.K. Allen, J.
795 Doschung, A. Nauels, Y. Xia, V. Bex, and P.M. Midgley, Eds. Cambridge University Press,
796 pp. 571-657, doi:10.1017/CBO9781107415324.016.
- 797 Davies, R., Á. Horváth, C. Moroney, B. Zhang, and Y. Zhu (2007), Cloud motion vectors from
798 MISR using sub-pixel enhancements, *Remote Sensing of Environment*, 107(1-2), 194–199,
799 doi:10.1016/j.rse.2006.09.023.
- 800 Davies, R., V. M. Jovanovic, and C. M. Moroney (2017), Cloud heights measured by MISR from
801 2000 to 2015, *Journal of Geophysical Research: Atmospheres*, 122(7), 3975–3986,
802 doi:10.1002/2017jd026456.
- 803 Dufresne, J.-L., and S. Bony (2008), An Assessment of the Primary Sources of Spread of Global
804 Warming Estimates from Coupled Atmosphere–Ocean Models, *Journal of Climate*, 21(19),
805 5135–5144, doi:10.1175/2008jcli2239.1.
- 806 Eastman, R., and S. G. Warren (2014), Diurnal Cycles of Cumulus, Cumulonimbus, Stratus,
807 Stratocumulus, and Fog from Surface Observations over Land and Ocean, *Journal of*
808 *Climate*, 27(6), 2386–2404, doi:10.1175/jcli-d-13-00352.1.
- 809 Geiss, A., and R. Marchand (2019), Cloud responses to climate variability over the extratropical
810 oceans as observed by MISR and MODIS, *Atmospheric Chemistry and Physics*, 19(11),
811 7547–7565, doi:10.5194/acp-19-7547-2019.
- 812 Harshvardhan, G. Zhao, L. D. Girolamo, and R. Green (2009), Satellite-Observed Location of
813 Stratocumulus Cloud-Top Heights in the Presence of Strong Inversions, *IEEE Transactions*
814 *on Geoscience and Remote Sensing*, 47(5), 1421–1428, doi:10.1109/tgrs.2008.2005406.
- 815 Holz, R. E., S. A. Ackerman, F. W. Nagle, R. Frey, S. Dutcher, R. E. Kuehn, M. A. Vaughan, and
816 B. Baum (2008), Global Moderate Resolution Imaging Spectroradiometer (MODIS) cloud
817 detection and height evaluation using CALIOP, *Journal of Geophysical Research*, 113,
818 doi:10.1029/2008jd009837.
- 819 Hong, Y., and L. Di Girolamo (2020), Cloud phase characteristics over Southeast Asia from A-
820 Train satellite observations, *Atmospheric Chemistry and Physics*, 20(13), 8267–8291,
821 doi:10.5194/acp-20-8267-2020.
- 822 Horváth, Á. (2013), Improvements to MISR stereo motion vectors, *Journal of Geophysical*

- 823 *Research: Atmospheres*, 118(11), 5600–5620, doi:10.1002/jgrd.50466.
- 824 Jovanovic, V., C. Moroney, and D. Nelson (2007), Multi-angle geometric processing for globally
825 geo-located and co-registered MISR image data, *Remote Sensing of Environment*, 107(1-2),
826 22–32, doi:10.1016/j.rse.2006.08.013.
- 827 Li, J., J. Huang, K. Stamnes, T. Wang, Q. Lv, and H. Jin (2015), A global survey of cloud overlap
828 based on CALIPSO and CloudSat measurements, *Atmospheric Chemistry and Physics*, 15(1),
829 519–536, doi:10.5194/acp-15-519-2015.
- 830 Lonitz, K., and Á. Horváth (2011), Comparison of MISR and Meteosat-9 cloud-motion
831 vectors, *Journal of Geophysical Research: Atmospheres*, 116(D24),
832 doi:10.1029/2011jd016047.
- 833 Marchand, R. T., T. P. Ackerman, and C. Moroney (2007), An assessment of Multiangle Imaging
834 Spectroradiometer (MISR) stereo-derived cloud top heights and cloud top winds using
835 ground-based radar, lidar, and microwave radiometers, *Journal of Geophysical
836 Research*, 112(D6), doi:10.1029/2006jd007091.
- 837 Marchand, R. (2012), Spatial correlation of hydrometeor occurrence, reflectivity, and rain rate
838 from CloudSat, *Journal of Geophysical Research: Atmospheres*, 117(D6),
839 doi:10.1029/2011jd016678.
- 840 Marchant, B., S. Platnick, K. Meyer, G. T. Arnold, and J. Riedi (2016), MODIS Collection 6
841 shortwave-derived cloud phase classification algorithm and comparisons with
842 CALIOP, *Atmospheric Measurement Techniques*, 9(4), 1587–1599, doi:10.5194/amt-9-
843 1587-2016.
- 844 McGill, M. J., J. E. Yorks, V. S. Scott, A. W. Kupchock, and P. A. Selmer (2015), The Cloud-
845 Aerosol Transport System (CATS): a technology demonstration on the International Space
846 Station, *Lidar Remote Sensing for Environmental Monitoring XV*, doi:10.1117/12.2190841.
- 847 Menzel, W. P., R. A. Frey, and B. A. Baum (2015), Cloud Top Properties And Cloud Phase
848 Algorithm Theoretical Basis Document Collection 006 Update. [Available at
849 [https://atmosphere-imager.gsfc.nasa.gov/sites/default/files/ModAtmo/MOD06-
850 ATBD_2015_05_01_1.pdf](https://atmosphere-imager.gsfc.nasa.gov/sites/default/files/ModAtmo/MOD06-ATBD_2015_05_01_1.pdf)],
- 851 Menzel, W. P., W. L. Smith, and T. R. Stewart (1983), Improved Cloud Motion Wind Vector and
852 Altitude Assignment Using VAS, *Journal of Climate and Applied Meteorology*, 22(3), 377–
853 384, doi:10.1175/1520-0450(1983)022<0377:icmwva>2.0.co;2.
- 854 Menzel, W. P., R. A. Frey, H. Zhang, D. P. Wylie, C. C. Moeller, R. E. Holz, B. Maddux, B. A.
855 Baum, K. I. Strabala, and L. E. Gumley (2008), MODIS Global Cloud-Top Pressure and
856 Amount Estimation: Algorithm Description and Results, *Journal of Applied Meteorology and
857 Climatology*, 47(4), 1175–1198, doi:10.1175/2007jamc1705.1.
- 858 Moroney, C., R. Davies, and J.-P. Muller (2002), Operational retrieval of cloud-top heights using
859 MISR data, *IEEE Transactions on Geoscience and Remote Sensing*, 40(7), 1532–1540,

860 doi:10.1109/tgrs.2002.801150.

861 Mueller, K. J., C. P. Moroney, V. Jovanovic, J.-P. Muller, L. Di Girolamo, and R. Davies (2013),
862 MISR Level 2 Cloud Product Algorithm Theoretical Basis. [Available at
863 https://eosps0.gsfc.nasa.gov/sites/default/files/atbd/MISR_L2_CLOUD_ATBD-1.pdf].

864 Mueller, K. J., D. L. Wu, Á. M. Horváth, V. M. Jovanovic, J.-P. J. Muller, L. Di Girolamo, M. J.
865 Garay, D. J. Diner, C. Moroney, and S. Wanzong (2017), Assessment of MISR Cloud Motion
866 Vectors (CMVs) Relative to GOES and MODIS Atmospheric Motion Vectors
867 (AMVs), *Journal of Applied Meteorology and Climatology*, 56(3), 555–572,
868 doi:10.1175/jamc-d-16-0112.1.

869 Muller, J.-P., A. Mandanayake, C. Moroney, R. Davies, D. Diner, and S. Paradise (2002), MISR
870 stereoscopic image matchers: techniques and results, *IEEE Transactions on Geoscience and*
871 *Remote Sensing*, 40(7), 1547–1559, doi:10.1109/tgrs.2002.801160.

872 National Academies of Sciences, Engineering, and Medicine. 2018. *Thriving on Our Changing*
873 *Planet: A Decadal Strategy for Earth Observation from Space*. Washington, DC: The
874 National Academies Press. doi: <https://doi.org/10.17226/24938>.

875 Naud, C., B. Baum, M. Pavolonis, A. Heidinger, R. Frey, and H. Zhang (2007), Comparison of
876 MISR and MODIS cloud-top heights in the presence of cloud overlap, *Remote Sensing of*
877 *Environment*, 107(1-2), 200–210, doi:10.1016/j.rse.2006.09.030.

878 Naud, C., J.-P. Muller, and E. E. Clothiaux (2002), Comparison of cloud top heights derived from
879 MISR stereo and MODIS CO2-slicing, *Geophysical Research Letters*, 29(16),
880 doi:10.1029/2002gl015460.

889 Naud, C., J.-P. Muller, M. Haeffelin, Y. Morille, and A. Delaval (2004), Assessment of MISR and
890 MODIS cloud top heights through inter-comparison with a back-scattering lidar at SIRTa,
891 *Geophys. Res. Lett.*, 31, L04114, doi:10.1029/2003GL018976.

892 Ohring, G., B. Wielicki, R. Spencer, B. Emery, and R. Datta (2004), Satellite instrument
893 calibration for measuring global climate change, *Bulletin of the American Meteorological*
894 *Society*, 86(9), 1303–1313, doi:10.6028/nist.ir.7047.

895 Pauly, R. M. et al. (2019), Cloud-Aerosol Transport System (CATS) 1064 nm calibration and
896 validation, *Atmospheric Measurement Techniques*, 12(11), 6241–6258, doi:10.5194/amt-12-
897 6241-2019.

898 Platnick, S. et al. (2017), The MODIS Cloud Optical and Microphysical Products: Collection 6
899 Updates and Examples From Terra and Aqua, *IEEE Transactions on Geoscience and Remote*
900 *Sensing*, 55(1), 502–525, doi:10.1109/tgrs.2016.2610522.

901 Rajapakshe, C., Z. Zhang, J. E. Yorks, H. Yu, Q. Tan, K. Meyer, S. Platnick, and D. M. Winker
902 (2017), Seasonally transported aerosol layers over southeast Atlantic are closer to underlying
903 clouds than previously reported, *Geophysical Research Letters*, 44(11), 5818–5825,

904 doi:10.1002/2017gl073559.

905 Smith, W. L., and C. M. R. Platt (1978), Comparison of Satellite-Deduced Cloud Heights with
906 Indications from Radiosonde and Ground-Based Laser Measurements, *Journal of Applied*
907 *Meteorology*, 17(12), 1796–1802, doi:10.1175/1520-0450(1978)017<1796:cosdch>2.0.co;2.

908 Stubenrauch, C. J., and Coauthors (2013), Assessment of Global Cloud Datasets from Satellites:
909 Project and Database Initiated by the GEWEX Radiation Panel, *Bulletin of the American*
910 *Meteorological Society*, 94(7), 1031–1049, doi:10.1175/bams-d-12-00117.1.

911 Van Dienenhoven, B., A. M. Fridlind, B. Cairns, A. S. Ackerman, and J. E. Yorks (2016), Vertical
912 variation of ice particle size in convective cloud tops, *Geophysical Research Letters*, 43(9),
913 4586–4593, doi:10.1002/2016gl068548.

914 Vaughan, M. A., D. M. Winker, and K. A. Powell (2005), CALIOP Algorithm Theoretical Basis
915 Document Part 2: Feature Detection and Layer Properties Algorithms. PC-SCI-202 Part 2
916 Release 1.01. [Available at [https://www-calipso.larc.nasa.gov/resources/pdfs/PC-SCI-](https://www-calipso.larc.nasa.gov/resources/pdfs/PC-SCI-202_Part2_rev1x01.pdf)
917 [202_Part2_rev1x01.pdf](https://www-calipso.larc.nasa.gov/resources/pdfs/PC-SCI-202_Part2_rev1x01.pdf)],

918 Vaughan, M. A., K. A. Powell, D. M. Winker, C. A. Hostetler, R. E. Kuehn, W. H. Hunt, B. J.
919 Getzewich, S. A. Young, Z. Liu, and M. J. McGill (2009), Fully Automated Detection of
920 Cloud and Aerosol Layers in the CALIPSO Lidar Measurements, *Journal of Atmospheric*
921 *and Oceanic Technology*, 26(10), 2034–2050, doi:10.1175/2009jtecha1228.1.

922 Wielicki, B. A., and J. A. Coakley (1981), Cloud Retrieval Using Infrared Sounder Data: Error
923 Analysis., *Journal of Applied Meteorology*, 20(2), 157–169, doi:10.1175/1520-
924 0450(1981)020<0157:CRUISD>2.0.CO;2.

925 Wylie, D. P., and W. P. Menzel (1989), Two Years of Cloud Cover Statistics Using VAS, *Journal*
926 *of Climate*, 2(4), 380–392, doi:10.1175/1520-0442(1989)002<0380:tyoccs>2.0.co;2.

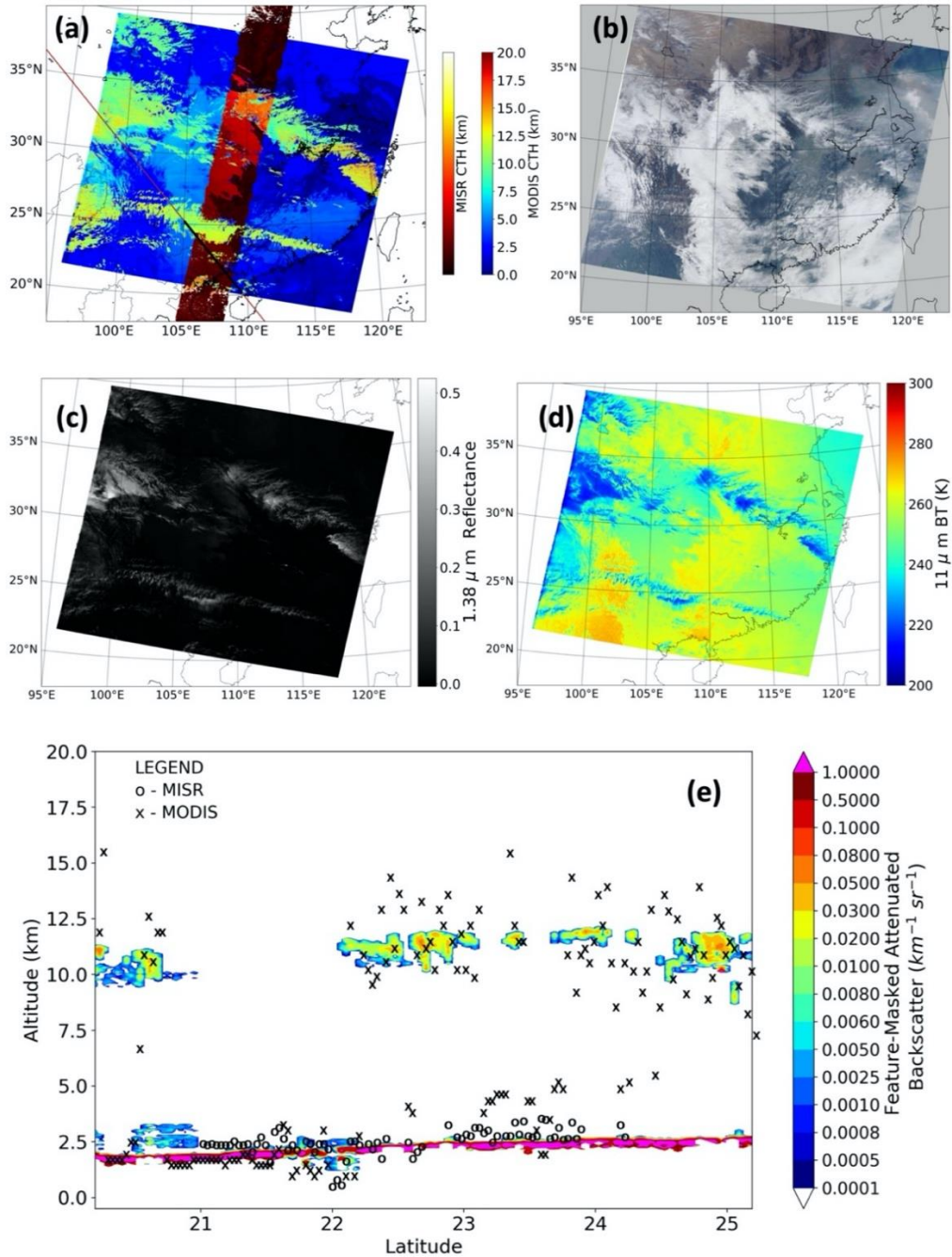
927 Yorks, J. E., S. P. Palm, D. L. Hlavka, M. J. McGill, E. D. Nowottnick, P. D. Selmer, and W.
928 undefined Hart (2016), The Cloud-Aerosol Transport System (CATS) algorithm theoretical
929 basis document. [Available at https://cats.gsfc.nasa.gov/media/docs/CATS_ATBD.pdf],

930 Yorks, J. E., M. J. McGill, S. P. Palm, D. L. Hlavka, P. A. Selmer, E. P. Nowottnick, M. A.
931 Vaughan, S. D. Rodier, and W. D. Hart (2016), An overview of the CATS level 1 processing
932 algorithms and data products, *Geophysical Research Letters*, 43(9), 4632–4639,
933 doi:10.1002/2016gl068006.

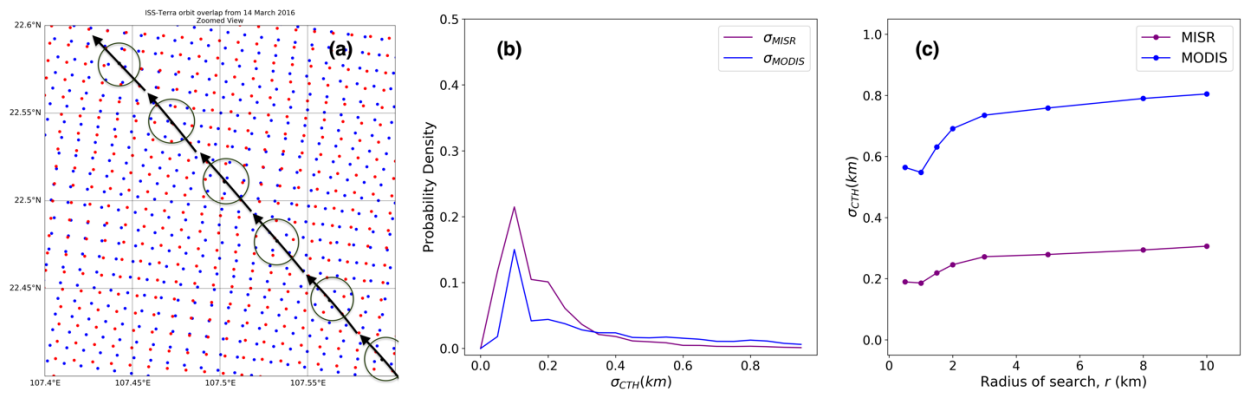
934 Zelinka, M. D., D. A. Randall, M. J. Webb, and S. A. Klein (2017), Clearing clouds of
935 uncertainty, *Nature Climate Change*, 7(10), 674–678, doi:10.1038/nclimate3402.

936 Zhao, G., L. Di Girolamo, D. J. Diner, C. J. Bruegge, K. L. Mueller, and D. Wu (2016), Regional
937 Changes in Earths Color and Texture as Observed From Space Over a 15-Year Period, *IEEE*
938 *Transactions on Geoscience and Remote Sensing*, 54(7), 4240–4249,
939 doi:10.1109/tgrs.2016.2538723.

941 **Figure 1.** A collocation case from 14 March 2016 over South-East Asia, between MODIS, MISR and CATS. (a)
 942 MODIS and MISR CTH. The part of the CATS orbit that was nearly coincident with MISR and MODIS is in black.
 943 (b) MODIS RGB. (c) MODIS 1.38 μ m Reflectance (d) MODIS 11 μ m Brightness Temperature (e) The vertical cross-
 944 section of attenuated backscatter of cloud layers as detected from CATS. The approximate MISR and MODIS CTH
 945 are also plotted. All CTH are with respect to the WGS84 ellipsoid.

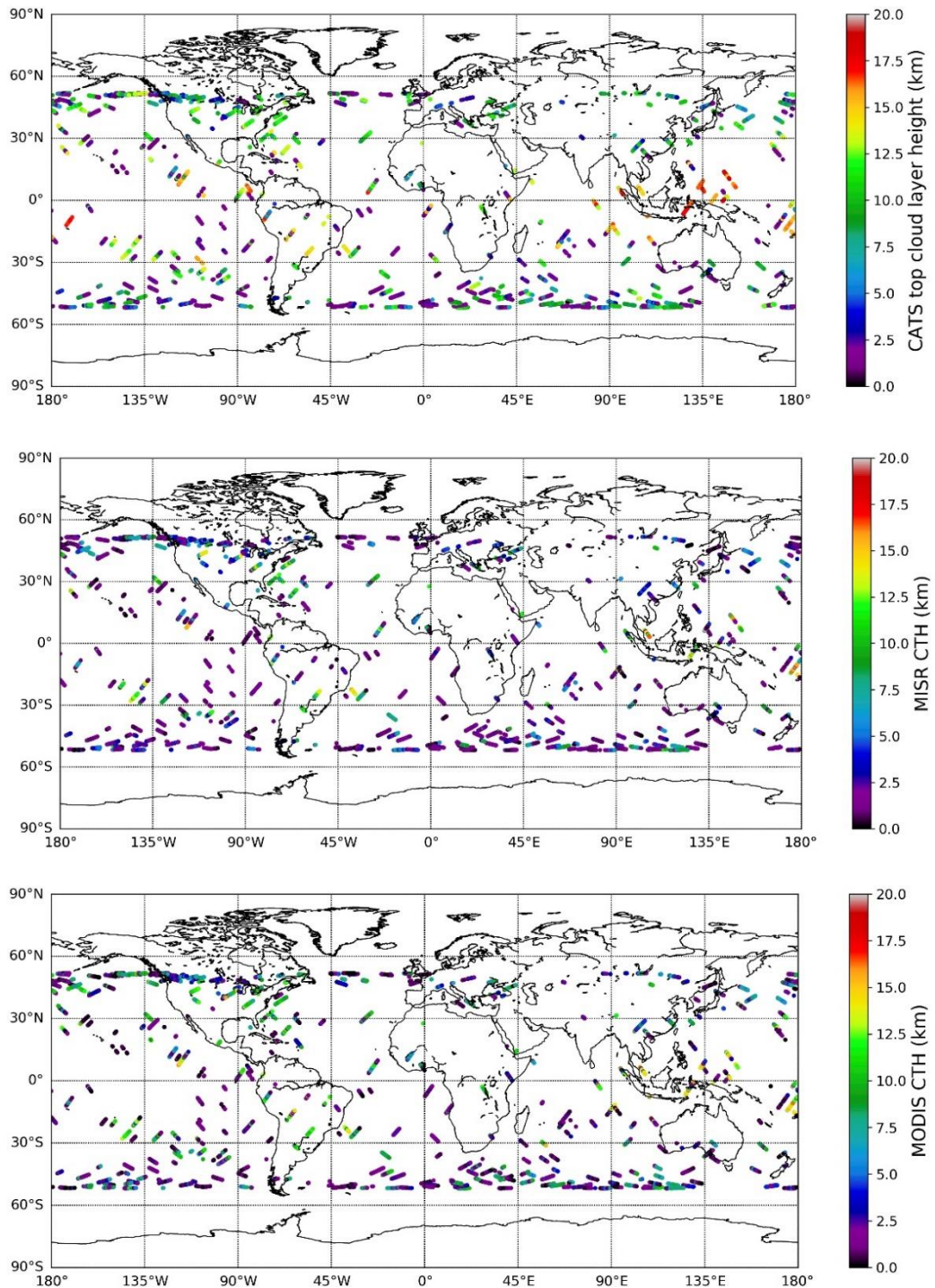


948 **Figure 2.** (a) A highly zoomed view of the collocation case from 14 March 2016, between MODIS, MISR and CATS,
 949 from Figure 1. MODIS geolocations are in blue, MISR in red. The black arrows signify the general direction and 5-
 950 km along-track extent of the CATS pixels, with the dark circles approximately signifying 1-km radii (not precisely to
 951 scale) from the CATS geolocation, within which the nearest neighboring MISR and MODIS pixels were searched;
 952 Histograms of the standard deviation of MISR (purple) and MODIS (blue) CTH within each 1-km radii search
 953 windows for all successful collocation incidents for the year 2016; (c) Mean standard deviation of MISR (purple) and
 954 MODIS (blue) CTH for progressively bigger search radii, for all successful collocation incidents from 2016.



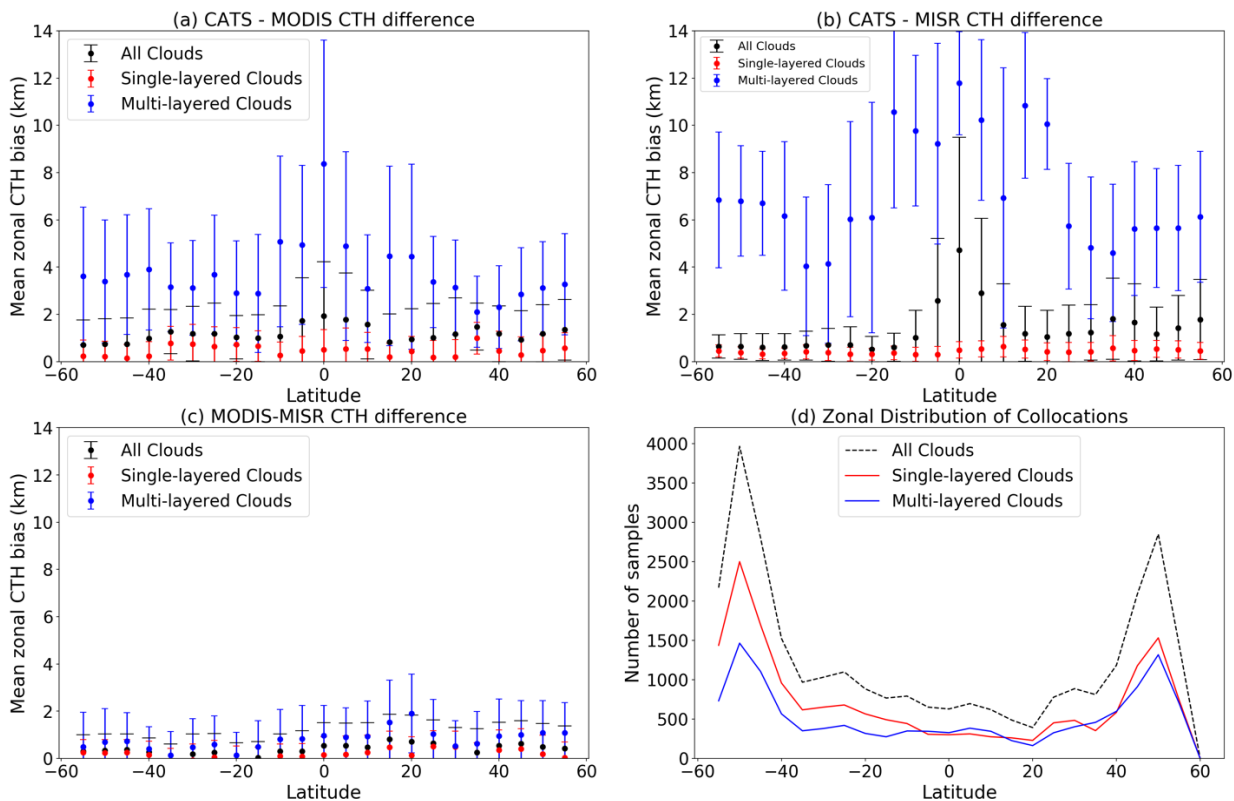
956

957 **Figure 3.** The global distribution of collocations of CATS, MISR and MODIS, where all three instruments recorded
958 valid cloud top height retrievals for all of CATS operation. 18,986 individual collocated points have been plotted in
959 the figure.



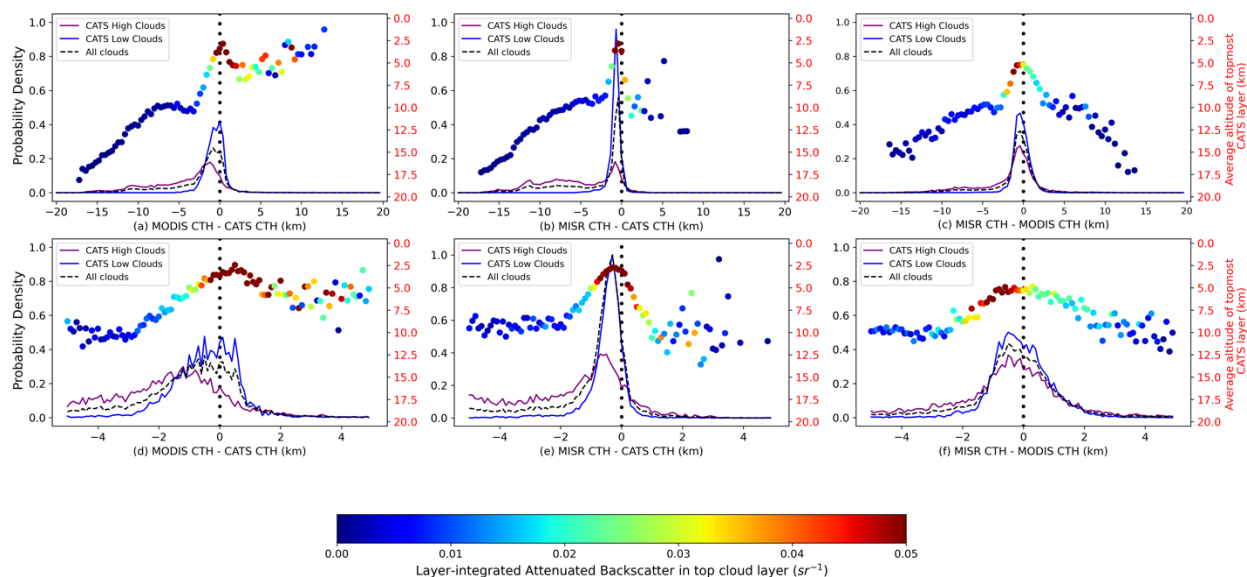
960
961
962

963 **Figure 4.** Latitudinal distribution of median CTH differences for CATS-MODIS (top left), CATS-MISR (top right),
 964 and MODIS-MISR (bottom left) for all clouds (black), CATS single-layered clouds (red) and CATS multi-layered
 965 clouds (blue). The number of samples in each latitudinal bin is shown in the bottom right panel. Error bars in the first
 966 three subplots represent the median absolute deviation statistic.
 967



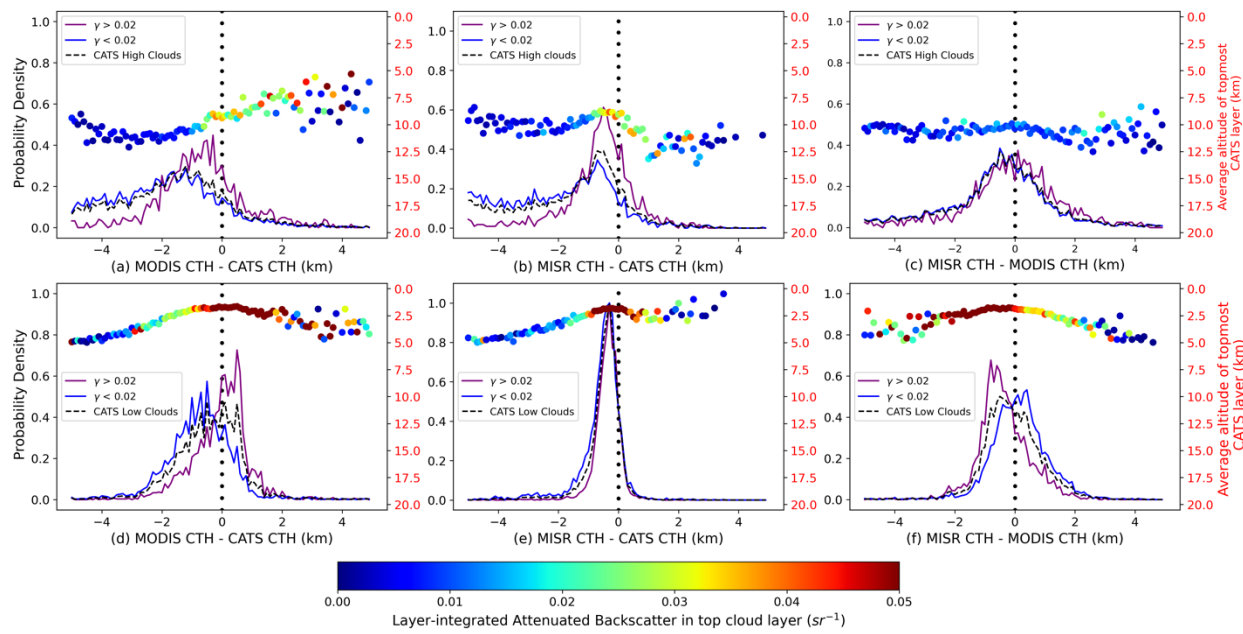
968

969 **Figure 5.** Histograms of global CTH differences for high clouds (CATS CTH > 5 km, purple) and low clouds (CATS
 970 CTH < 5 km, blue), with 100 bins between +20 km and -20 km (top panels) and +5 km and -5 km (bottom panels)
 971 The overall distribution is marked by a black dashed line and contains 18986 collocated data points, out of which
 972 10315 were high clouds. For each histogram bin, the average CATS top layer height has been marked in an inverted
 973 system of axes in red, with each point denoting the CATS layer-integrated backscatter (γ) for the topmost cloud layer.



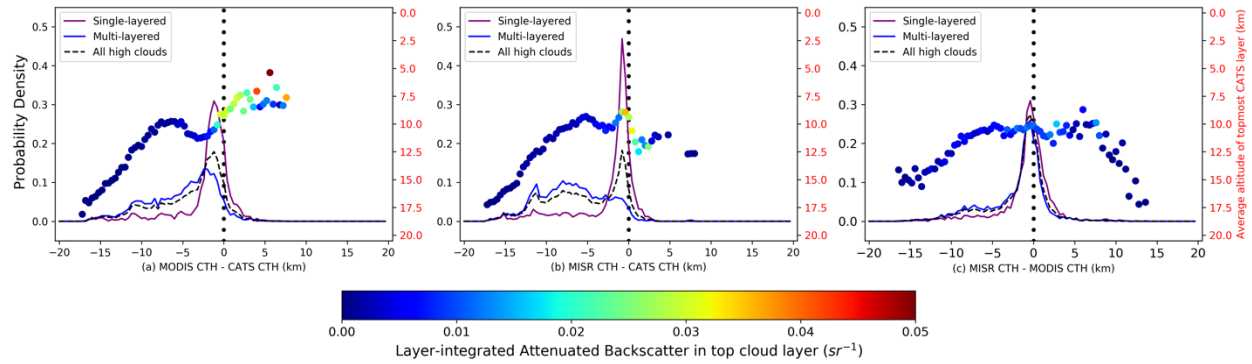
974

975 **Figure 6.** Histograms of global CTH differences for (a-c) high clouds and (d-f) low clouds from CATS, for optically
 976 thick top layer of cloud ($\gamma > 0.02 \text{ sr}^{-1}$, purple) and optically thin top layer of cloud ($\gamma < 0.02 \text{ sr}^{-1}$, blue), with the black
 977 dashed line denoting overall distributions.
 978



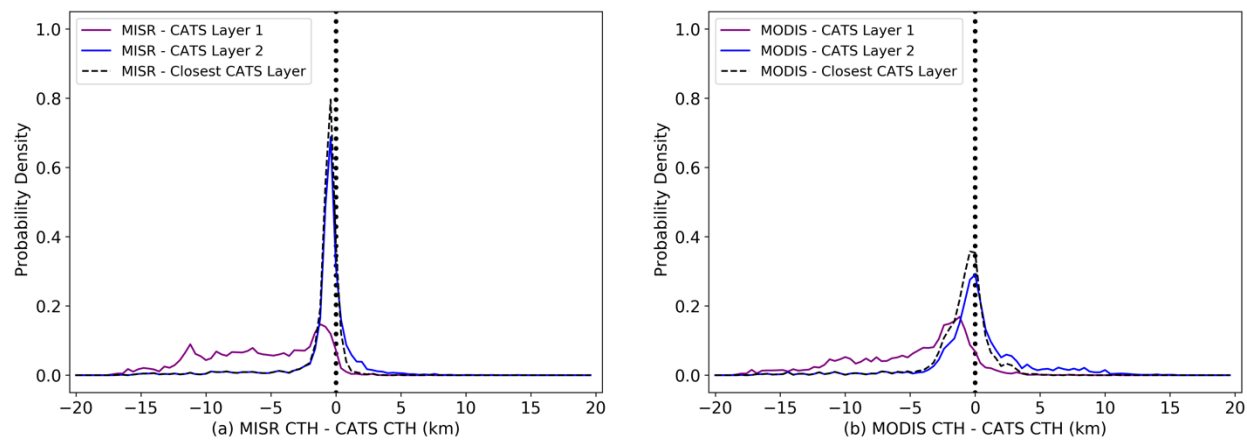
979
 980

981 **Figure 7.** Histograms of global CTH differences for CATS single-layered clouds (CATS Percentage Opacity < 50%,
982 purple) and multi-layered clouds (CATS detected at least two layers, blue), with the CATS top layer height being
983 greater than 5 km.
984



985
986

987 **Figure 8.** Histograms of global CTH differences for double-layered clouds from CATS, for each passive sensor – (a)
988 MISR and (b) MODIS - and the first layer (blue) and second layer (red) of CATS clouds, respectively, with 100 bins
989 between +20 km and -20 km. The distribution of the difference in cloud top height from each passive sensor and the
990 closest CATS layer is given by a black dashed line and contains 7454 collocated data points.



991
992

993 **Table 1.** MODIS and MISR CTH bias and precision (rounded to the nearest multiple of 10) with respect to CATS,
 994 summarizing Sections 4.2-4.4. In each row, MISR and MODIS errors are probed by imposing conditions on a cloud
 995 “parameter of interest” (e.g., top-layer height), thus extracting from our dataset a subset of scenes that is representative
 996 of a “type of cloud” (e.g., high/low).
 997

| Parameter of Interest | Type of Cloud | MODIS | | MISR | |
|--------------------------------|---|----------|---------------|----------|---------------|
| | | Bias (m) | Precision (m) | Bias (m) | Precision (m) |
| Topmost Cloud-Layer Height | High (CATS CTH > 5km) | -1200 | 1080 | -540 | 590 |
| | Low (CATS CTH < 5km) | 40 | 730 | -320 | 250 |
| Topmost Cloud OD (High clouds) | Optically thick ($\gamma > 0.02 \text{ sr}^{-1}$) | -280 | 730 | -440 | 470 |
| | Optically thin ($\gamma < 0.02 \text{ sr}^{-1}$) | -1160 | 1020 | -680 | 550 |
| Topmost Cloud OD (Low clouds) | Optically thick ($\gamma > 0.02 \text{ sr}^{-1}$) | 500 | 430 | -280 | 260 |
| | Optically thin ($\gamma < 0.02 \text{ sr}^{-1}$) | -440 | 600 | -320 | 310 |
| Cloud Overlap | Single-layered (High) | -1160 | 510 | -720 | 460 |
| | Multi-layered (Highest layer) | -2380 | 1030 | N/A* | N/A* |
| | Multi-layered (Top Layer Closest) | -1200 | 1190 | -820 | 850 |
| | Multi-layered (Bottom Layer Closest) | 20 | 850 | -400 | 350 |

998 *Distribution does not resemble Gaussian.

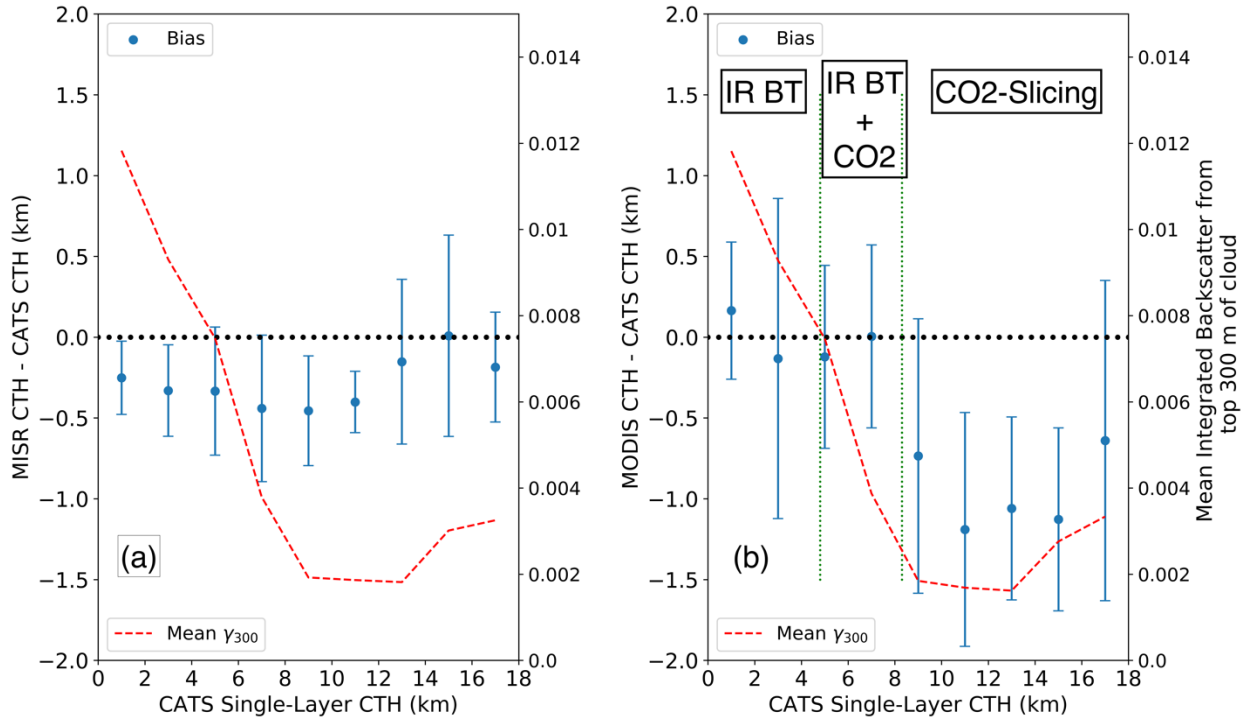
999
 1000

1001 **Table 2.** MISR and MODIS bias and precision (rounded to nearest multiple of 10) for all, high, mid-level and low
 1002 clouds, as seen by CATS, with absolute CTH difference with respect to CATS ≤ 2.5 km and CATS Percentage Opacity
 1003 = 1.
 1004

| Instrument | Overall | | High (CATS CTH > 10 km) | | Mid-level (10 km > CTH > 5 km) | | Low (CATS CTH < 5 km) | |
|--------------|----------|---------------|-------------------------|---------------|--------------------------------|---------------|-----------------------|---------------|
| | Bias (m) | Precision (m) | Bias (m) | Precision (m) | Bias (m) | Precision (m) | Bias (m) | Precision (m) |
| MISR | -280 | 370 | -300 | 400 | -370 | 400 | -240 | 300 |
| MODIS | -540 | 690 | -950 | 740 | -350 | 690 | 60 | 660 |

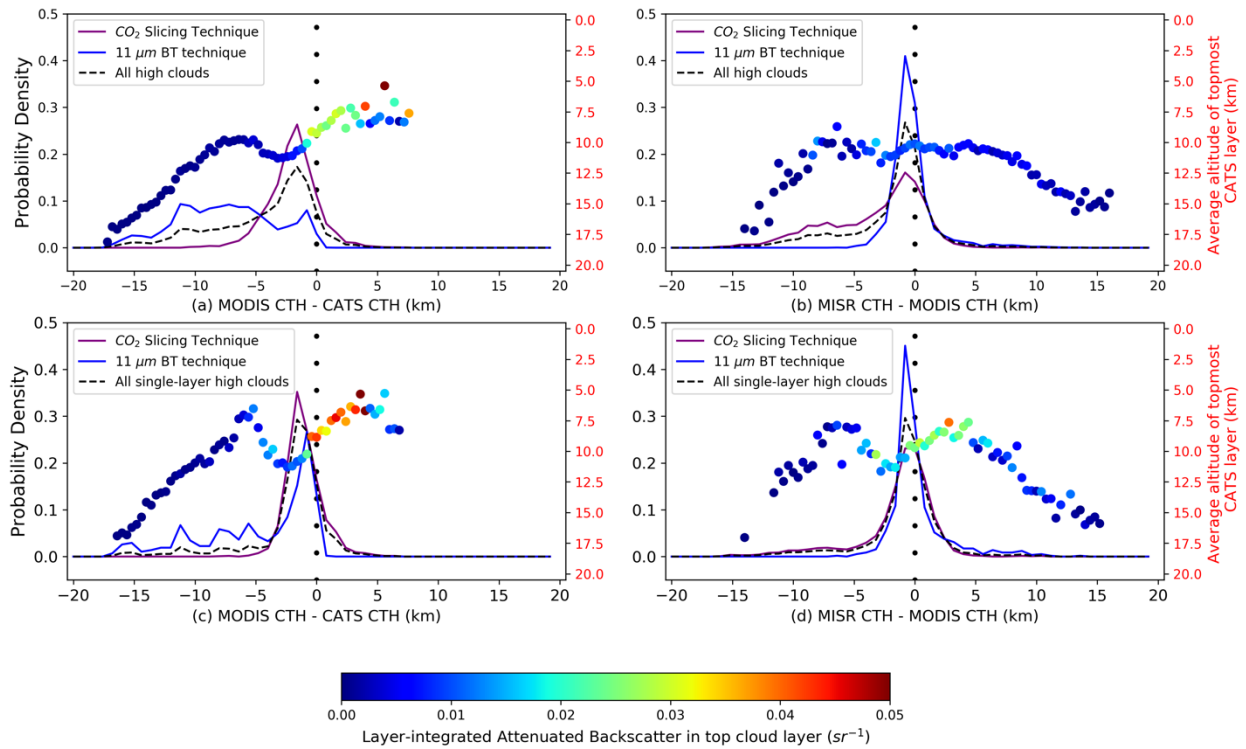
1005
 1006

1007 **Figure 9.** Distribution with altitude of (a) MISR and (b) MODIS CTH bias and precision (1σ error-bars) for CATS
 1008 single-layered clouds with Percentage Opacity = 1 and an absolute CTH difference ≤ 2.5 km. The results are binned
 1009 every 2 km (bin centers are odd integers), with mean CATS integrated backscatter for the top 300 m into the cloud
 1010 (γ_{300} in sr^{-1}) shown in red. Green dotted lines in (b) denote the 75th-percentile CATS CTH for scenes employing IR
 1011 BT (left line) and CO₂-slicing, respectively. Each bin has a minimum of 150 samples.



1012

1013 **Figure 10.** Histograms of global CTH differences for CATS high (CTH > 5 km) clouds (upper panel) and CATS
 1014 single-layered high clouds (lower panel). CO₂ retrievals are in purple and 11- μ m brightness temperature retrievals are
 1015 in blue. For each histogram bin of CTH difference, the average CATS top layer height has been marked in an inverted
 1016 system of axes in red, with each point denoting the layer-integrated CATS backscatter for the topmost cloud layer.



1017